Pratik P. Dholabhai\*

School of Physics and Astronomy Rochester Institute of Technology

Rochester, NY 14623

\* Email: pratik.dholabhai@rit.edu

Title: Correction to "Oxygen Vacancy Formation and Interface Charge Transfer at Misfit

Dislocations in Gd-doped CeO<sub>2</sub>/MgO Heterostructure"

Pratik P. Dholabhai

J. Phys. Chem. C 2022, 126 (28), 11735–11750

https://doi.org/10.1021/acs.jpcc.2c02009

In the published version of the paper, the Acknowledgments was incomplete as the National

Science Foundation (NSF) CAREER Award grant number 2042311 was acknowledged, whereas

the complete award number is DMR-2042311. The author apologizes for any inconvenience that

it may have caused. The correct acknowledgment is given below:

This work is supported by the National Science Foundation (NSF) CAREER Award grant

number DMR-2042311 in the Division of Materials Research. This work used Extreme Science

and Engineering Discovery Environment (XSEDE), which is supported by NSF grant number

ACI-1548562. The authors acknowledge partial computing resources from Research Computing

at the Rochester Institute of Technology.

1

# Oxygen Vacancy Formation and Interface Charge Transfer at Misfit Dislocations in Gd-doped CeO<sub>2</sub>/MgO Heterostructure

Pratik P. Dholabhai\*

School of Physics and Astronomy Rochester Institute of Technology Rochester, NY 14623

#### Abstract

Among numerous functionalities of mismatched complex oxide thin films and heterostructures, their application as next-generation electrolytes in solid oxide fuel cells have shown remarkable promise. In thin film oxide electrolytes, although misfit dislocations ubiquitous at interfaces play a critical role in ionic transport, fundamental understanding of their influence on oxygen vacancy formation and passage is nevertheless lacking. Herein, we report first principles density functional theory calculations to elucidate the atomic and electronic structure of misfit dislocations in CeO<sub>2</sub>/MgO heterostructure for the experimentally observed epitaxial relationship. Thermodynamic stability of the structure corroborates recent results demonstrating that the 45° rotation of CeO<sub>2</sub> thin film eliminates the surface dipole resulting in experimentally observed epitaxy. The energetics and electronic structure of oxygen vacancy formation near gadolinium dopants at misfit dislocations is evaluated, which demonstrate complex tendencies as compared to the grain interior and surfaces of ceria. Interface charge transfer mechanism is studied for defect-free and defective interfaces. Since the atomic and electronic structure of misfit dislocations at complex oxide interfaces and their influence on interface charge transfer and oxygen vacancy defect formation has not been studied in the past, this work offers new opportunities to unravel the untapped potential of oxide heterostructures.

**Keywords**: solid oxide fuel cells, oxide electrolytes, doped ceria, misfit dislocations, electronic structure

\* Email: pratik.dholabhai@rit.edu

## 1. Introduction

Owing to the ever-growing miniaturization of emerging nanotechnologies, the role of interfaces has never been more critical. Mismatched oxide heterostructures exhibit superior properties as compared to their individual constituents. 1,2,3,4,5 In these properties, heterointerfaces play a crucial role in influencing novel behavior for diverse applications in Solid Oxide Fuel Cells (SOFCs), 6,7,8 batteries, 9 nuclear materials, catalysis, 10 solar cells, 11 and information storage. 12,13 At the interfaces of semi-coherent oxide heterostructures, mismatch between the film and the substrate result in formation of microstructural feature known as misfit dislocations, which mitigate the mismatch strain.<sup>14</sup> High interface to volume ratio in oxide heterostructures result in high density of misfit dislocations. Consequently, the role of misfit dislocations in semicoherent oxide heterostructures have been examined for applications as fast ionic conductors in SOFCs, 15,16,17,18,19,20,21,22,23,24 radiation damage in nuclear materials, 25,26,27 ferroelectrics, 28,29 transparent conducting semiconductors, 30 and catalysis. 31 Nonetheless, the influence of misfit dislocations on properties pertinent to these applications is not clear.<sup>32,33</sup> Besides, little is known about the basic role of extended defects (misfit dislocations) and their intricate interaction with points defects and dopants, which are pervasive at oxide heterointerfaces and are expected to influence aforementioned applications.

SOFCs are a promising technology for reducing carbon footprint, but their widespread implementation require lowering the operating temperatures to intermediate-temperature (IT-SOFC) range of 773–973 K.<sup>34,35,36,37</sup> Oxide thin films and heterostructures are often touted as the next-generation electrolytes for use in IT-SOFCs since they exhibit enhanced performance at these low temperatures.<sup>6,7,8,15,16,17,18,19,20,21,22,23,34,36</sup> One major hurdle in using thin film oxide electrolytes in IT-SOFCs is that the fundamental atomistic mechanisms responsible for ionic transport across oxide interfaces, specifically at misfit dislocations, are not apparent. This potential lack of clarity exists due to polarized results with some experiments hypothesizing misfit dislocations as pathways for fast ionic transport,<sup>6,7,8,15,16,17,18,19,20,21</sup> whereas others do not report such enhancement.<sup>22,23,38,39</sup> Adding to the ambiguity, computational studies report that homophase dislocations <sup>40,41</sup> and misfit dislocations <sup>24</sup> hamper oxide ion conductivity.

One of the most widely used electrolyte in SOFCs is doped ceria (CeO<sub>2</sub>), an extrinsic ionic conductor, wherein aliovalent dopants replacing tetravalent sites result in formation of oxygen vacancies that are largely responsible for higher ionic conductivity. 36,42,43,44,45,46,47,48,49,50

The resulting enhanced ionic conductivity in doped ceria is sensitive to the dopant type and fraction. 42,43,44,51,52,53,54,55,56,57,58,59,60 The intricate interplay between trivalent dopants and oxygen vacancies is well understood in the bulk, 42,43,44,52,53,57 and fundamental mechanisms for the optimal performance of doped ceria-based oxide electrolytes are well documented. 51,57,59,60 Nonetheless, the same is not true for doped ceria-based thin films and heterostructures.

Depending on processing conditions, possible features altered at oxide interfaces as compared to the bulk are chemical composition and stoichiometry.<sup>61</sup> In addition, the presence of dopants, <sup>62,63,64,65</sup> point defects, <sup>66,67,68</sup> and structural defects<sup>26,27</sup> result in a complex interplay between point defects, dopants, and misfit dislocations at oxide heterostructures. Proclivity of oxygen vacancies in doped ceria to exist at first, second or third nearest neighbor (NN) position relative to the dopant <sup>51,52,58,60,69</sup> result in stable complexes at low temperatures, which ultimately influence oxide ion conductivity. While dopants segregation at misfit dislocations is not well understood, it is anticipated to impact interface-governed properties. Recently, we established that oxygen vacancy segregation <sup>24,25</sup> and dopant segregation <sup>62</sup> in oxide heterostructures is influenced by atomic-layer chemistry and structure of misfit dislocations, further showing the importance of understanding the interplay between vacancies, dopants, and misfit dislocations. Although dopant-defect complexes are expected to occur at misfit dislocations and influence ionic conductivity across interfaces, not much is known about their structure and energetics.

Since doped ceria is an excellent ionic conductor, oxide heterostructures synthesized using ceria and doped ceria thin films deposited on MgO substrates have been extensively studied.  $^{70,71,72,73,74,75}$  Lattice constants of CeO<sub>2</sub> and MgO are vastly different with a mismatch of roughly 28.4%. Experimentally, for cube-on-cube epitaxy, the large lattice mismatch between doped ceria and MgO result in an almost continuous line of misfit dislocations that mitigate the stress at the interface.  $^{70,72,74}$  Conversely, there are studies that have not reported the presence of misfit dislocations at the CeO<sub>2</sub>/MgO interface, although the strain relieving mechanisms in such cases are not clear.  $^{71,73,75}$  There are two competing in-plane orientations for CeO<sub>2</sub>/MgO interface, [100] $_{CeO_2}$ ||[100] $_{MgO}$ ||Interface and [110] $_{CeO_2}$ ||[100] $_{MgO}$ ||Interface, wherein the latter has lower interfacial energy.  $^{71,73}$  Upon rotation of CeO<sub>2</sub> around the surface normal by 45°,  $^{71,72}$  the epitaxial misfit decreases to roughly 9.1% for the [110] $_{CeO_2}$ ||[100] $_{MgO}$ ||Interface orientation relationship. Irrespective of the epitaxial relationship, it is evident that the mismatch at the

CeO<sub>2</sub>/MgO interface is quite large, indicating that misfit dislocations would be present at the interfaces to relieve the large coherency strain.<sup>70,72,74</sup>

From a fundamental and technological standpoint, although the importance of misfit dislocations in semi-coherent CeO<sub>2</sub>/MgO heterostructures is unambiguous, their atomic and electronic structure and thermodynamic stability are not well understood. From experiments, basic information regarding atomic-scale structure of individual column of atoms in the neighborhood of misfit dislocations is not easily accessible due to buried heterointerfaces and metastable heterostructures encountered during synthesis. In computational studies, <sup>76</sup> the key challenge in simulating misfit dislocations in semi-coherent oxide heterostructures is to employ very large supercells so as to include fully relaxed thin films deposited on mismatched substrates.<sup>25</sup> In order to decrease supercell size and computational cost, density functional theory (DFT) studies 77,78,79 focused on coherent and strained oxide heterostructures mostly neglect the presence of misfit dislocations.<sup>76</sup> As a result, atomistic simulations based on empirical potentials has often been the method of choice to study misfit dislocations.<sup>80</sup> That said, neither can this approach offer information pertaining to the electronic structure of misfit dislocations and oxygen vacancies, nor can it provide any insights into electronic charge transfer across the heterointerface, all of which are critical to gain a holistic understanding of the role of misfit dislocations in shaping ionic transport across oxide heterostructures.

Herein, we report first principles DFT calculations to predict the atomic scale structure of misfit dislocations in CeO<sub>2</sub>/MgO heterostructures and elucidate the experimentally observed mixed epitaxial relationship. We further examine the atomic structure and stability of oxygen vacancies and gadolinium dopants in the neighborhood of misfit dislocations. Complex misfit dislocation structure, asymmetry, strain, and the availability of diverse nearest neighbor bonding environments between dopants and oxygen vacancy defects at the interface are responsible for a mix of exothermic and endothermic vacancy formation energies. We further shed light on the electronic structure of the interface and electronic charge transfer at the interface. Notably, results herein shed light on the importance of understanding the intricate interplay between dopants, defects, and extended defects. Fundamental first principles-based insights offered in this work, with primary focus on misfit dislocations in oxide heterostructures, have not been reported in the past, and offer the prospect of tuning ionic transport in thin film oxide electrolytes.

# 2. Methodology

# 2.1 Computational details

For all the cases considered, spin-polarized calculations were performed using the generalized gradient approximation (GGA) to DFT 81,82 with the Perdew-Burke-Ernzerhof (PBE)<sup>83</sup> exchange correlation functional. Within the GGA formalism, the Kohn-Sham equations were solved using the plane wave basis and used with projected augmented wave (PAW)84 method as implemented in the Vienna ab initio Simulation Package (VASP).85,86 To account for the strong on-site Coulomb repulsion amid the localized Ce 4f electrons, the rotationally invariant form of GGA+U,87 a combination of the standard GGA and a Hubbard Hamiltonian for the Coulomb repulsion and exchange interaction, was utilized. This method ensures accurate description of Ce 4f electrons and is well known to reproduce accurate electronic structure and defect behavior in ceria. A  $U_{\rm eff}$  value of 5.0 eV  $^{43,44}$  was applied to account for strong on-site Coulomb repulsion amid localized Ce 4f electrons. This value of  $U_{\rm eff}$  has been used within the GGA+U formalism before for studying ceria and doped ceria. 43,44 To ensure accurate results, a plane-wave cutoff energy of 400 eV was utilized, which converged the energies to approximately 0.01 meV. Ground state geometries of different systems were obtained by minimizing the Hellman-Feynman forces until the total forces on each atom were less than 0.02 eV/Å. The irreducible Brillouin-zone integrations were performed using Monkhorst–Pack grid<sup>88</sup> of 2 × 2 × 1 with Gaussian smearing of 0.1 eV. Large-scale DFT+U calculations were performed using the Extreme Science and Engineering Discovery Environment (XSEDE) resources.<sup>89</sup>

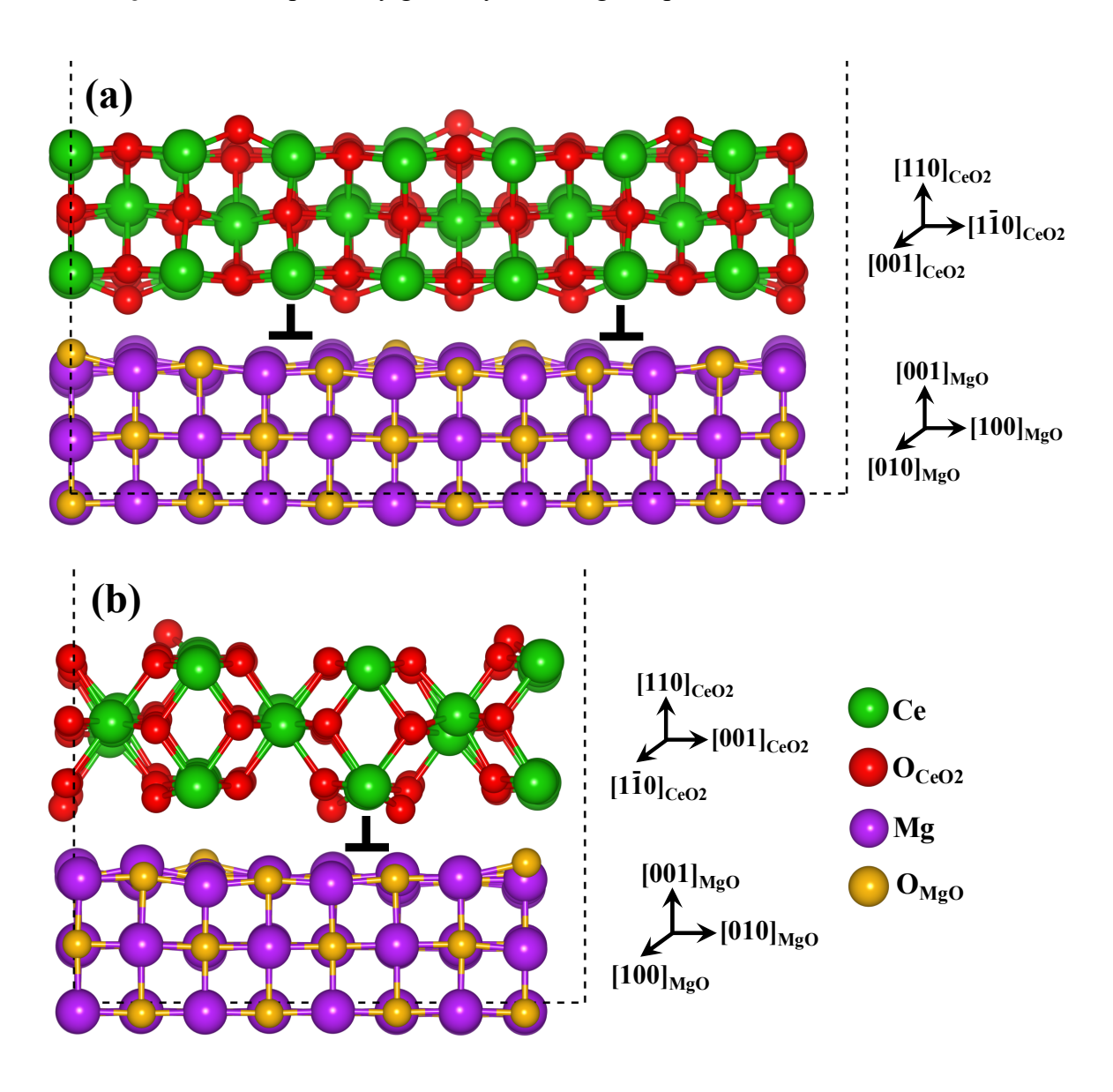
Since our work is primarily focused on 3D oxide heterostructures, we have not incorporated van der Waals (vdW) corrections in DFT calculations, which are pertinent to vdW heterostructures comprising of 2D materials, as well as important in cases where small molecules are interacting with oxide surfaces. Nonetheless, the DFT+U methodology used in this work is expected to capture fundamental aspects of atomic and electronic structures of oxide heterostructures, at least qualitatively. Importantly, the methodology used in this work has been fruitfully used for other complex oxide heterostructures, wherein the basic physical trends obtained from DFT+U are in good qualitative agreement with experimentally reported results. PFT+U are in good qualitative agreement with experimentally reported fidelity to provide physically meaningful trends that are in qualitative agreement with experiments.

#### 2.2 Model heterostructure

As reported in our previous work, 80 since the lattice parameters are  $a_{CeO2} = 0.5411$  nm and  $a_{\rm MgO} = 0.4212$  nm, the lattice mismatch resulting from cube-on-cube orientation relationship in CeO<sub>2</sub>/MgO is very large (~28.4%).<sup>70,71,72,73,74,75</sup> Alternating planes of Ce and O atoms in the CeO<sub>2</sub> [001] direction are responsible for the polar nature of the surface. We have demonstrated that rotation of CeO<sub>2</sub> thin film by 45° around the surface normal is one of the primary mechanisms to eliminate surface dipole in CeO<sub>2</sub>/MgO heterostructures, which explains the experimentally observed epitaxial relationship. 80 Due to this approach, strain along the [110] direction of the thin film is reduced to ~9.1%, whereas that along the [001] direction still remains ~28.4%. In order to incorporate this mismatch along two different crystallographic directions, very large supercells are needed, which can be easily handled using interatomic potentials based molecular dynamics (MD) simulations. 80 For instance, along the [110] direction of the thin film, 11 unit cells of  $CeO_2[1\overline{1}0]$  have to be matched with 10 unit cells of MgO[100]. Along the [001] direction of the thin film, 3 unit cells of CeO<sub>2</sub>[001] have to be matched with 4 unit cells of MgO[010]. Nonetheless, to keep the supercell tractable in DFT calculations, the film and the substrate were strained by 3% in the  $[1\bar{1}0]$  direction. That is, the film was contracted by 3% and the substrate was expanded by 3%. This approach allowed for matching of 7 unit cells of  $CeO_2[1\bar{1}0]$  with 6 unit cells of MgO[100] along the [1 $\bar{1}0$ ] direction, which ultimately decreased the number of atoms in the supercell. Along the [001] direction, the lattice parameter of the film and the substrate were not strained. The strain introduced in this manner, essential to maintain a manageable supercell size, primarily alters the misfit dislocation spacing along the [110] direction in comparison to the fully relaxed case. We expect that the fundamental properties of misfit dislocations would not be impacted by implementing this strategy, which has been implemented effectively in the literature. 91,92 Using this approach to predict the atomic scale structure of misfit dislocations, a stoichiometric 477-atom model of CeO<sub>2</sub>/MgO heterostructure with dimensions 2.521 × 1.659 × 2.598 nm<sup>3</sup> was built using the experimentally observed mixed epitaxial relationship of  $[1\bar{1}0]_{Ce02}||[100]_{Mg0}||Interface$  and  $[001]_{CeO2}||[010]_{MgO}||Interface$  (Figure 1). As depicted in Figure 1, the model contains three layers each of CeO<sub>2</sub> (189 atoms) and MgO (288 atoms). Since only three layers are implemented for the film and the substrate to limit the system size, a vacuum layer of 1.5 nm is introduced in the z-direction (supercell thickness) to avoid periodic interaction between misfit dislocations,

oxygen vacancies, and Gd dopants. This strategy ensures only one interface in the model. Periodic boundary conditions were implemented in all three directions in the supercell.

**Figure 1.** Side view of geometrically optimized CeO<sub>2</sub>/MgO heterostructure depicting atomic scale structure of misfit dislocations at the heterointerface along two different crystallographic directions (a)  $[1\bar{1}0]_{CeO_2}||[100]_{MgO}||Interface$  and (b)  $[001]_{CeO_2}||[010]_{MgO}||Interface$ . Green and purple spheres correspond to Ce and Mg ions, respectively. To offer contrast,  $O_{CeO_2}$  and  $O_{MgO}$  ions are respectively given by red and gold spheres.



# 2.3 Formalism for oxygen vacancy formation

The defect reaction governing the addition of trivalent dopants to ceria can be expressed in Kröger-Vink notation as:

$$M_2 O_3 \xrightarrow{CeO_2} 2M'_{Ce} + V_O^{"} + 3O_O^{\times}$$
 (1)

where  $V_0^{\circ}$  and M respectively represent the oxygen vacancy and trivalent dopant. Owing to ionic compensation, this reaction indicates that the substitution of two cerium ions with trivalent dopants will result in the formation of one oxygen vacancy. After the introduction of two trivalent dopants in bulk ceria, oxygen vacancy is formed at first nearest neighbor (1NN), 2NN, or 3NN to the dopant. 42,43,44,51,52,57 The NN distance criteria is given in our previous work. 80 Nevertheless, this basic defect reaction and oxygen vacancy formation at misfit dislocations in oxide heterostructures is not well understood. 80 Moreover, the electronic charge transfer at the heterointerface due to the formation of such dopant-defect complexes, while critical in governing ionic conductivity, have not received much attention from the scientific community. As this basic knowledge will be instrumental in designing next-generation thin film electrolytes, we address this key issue by studying the oxygen vacancy formation and associated electronic charge transfer in the vicinity of misfit dislocations. Due to their widespread use in ceria-based ionic conductors, we have used gadolinium as the representative case for trivalent dopants.  $^{36,42,44,46,48}$ 

In the supercell approach, the oxygen vacancy formation energy was calculated using

$$E_f = E_{DFT}(vac) - E_{DFT}(ideal) + \sum_i n_i \,\mu_i + q_{vac} E_F \qquad (2)$$

where  $E_{DFT}(vac)$  and  $E_{DFT}(ideal)$  are respective DFT total energies of the heterostructure with and without a vacancy defect;  $n_i$  is the number of atoms removed;  $\mu_i$  is the chemical potential of the species removed; q is the charge of the vacancy; and  $E_F$  is the Fermi energy. In this work, we are primarily focused on neutral oxygen vacancy defects that are formed to maintain the defect equilibria as given by **Equation 1**. As a result, the final term in **Equation 2** can be essentially neglected. Since only one oxygen is removed in each vacancy calculation, the third term in **Equation 2** is calculated as  $\frac{1}{2}E_{DFT}(O_2)$ . Here  $E_{DFT}(O_2)$  is the spin polarized total energy

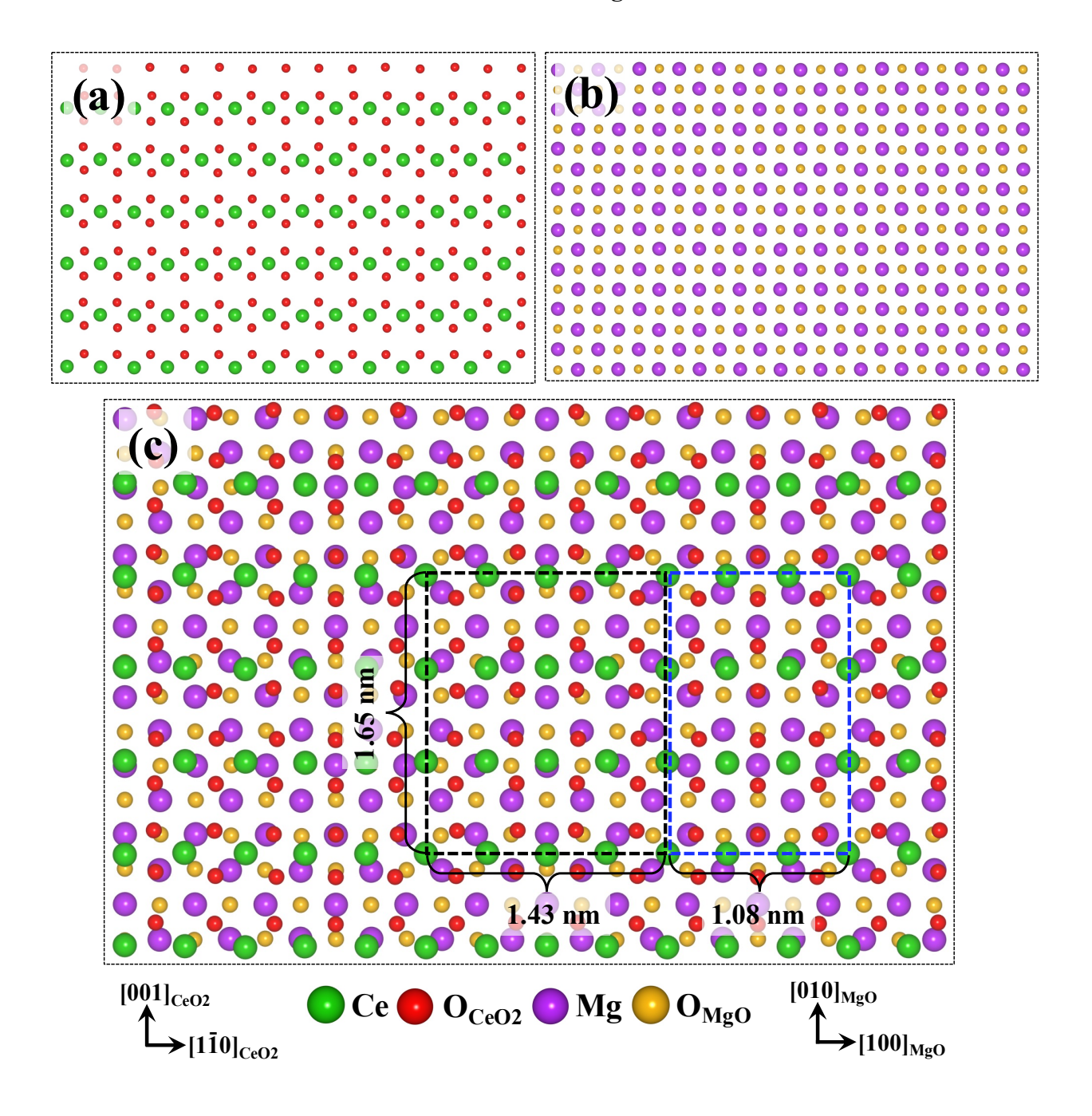
(chemical potential) for the ground state of an oxygen molecule in the gas phase calculated using the same supercell as that used for the heterostructure. Although this approach could possibly introduce a small error in the calculation of oxygen chemical potential, the overall qualitative trends for location preference of oxygen vacancy formation are not expected to alter. Importantly, this approach has been successfully implemented in the past to study oxygen vacancy formation energies in a wide variety of oxides. 42,43,44,60,95,96,97,99,100,101 For evaluating the oxygen vacancy formation in Gd-doped ceria, after their inclusion, energy minimization was performed wherein the ionic positions and supercell shape were allowed to fully relax prior to computing the formation energies. Throughout the calculations, the volume was held constant at the supercell volume without the oxygen vacancy, which is a reasonable approximation. 42,43,44

## 3. Results and discussion

## 3.1. Atomic-scale structure of the interface

Figure 1 shows the geometrically optimized and energetically minimized stoichiometric 477-atom CeO<sub>2</sub>/MgO heterostructure having the experimentally observed epitaxial relationship. Figure 1(a) and 1(b) respectively depict the side view of the supercell, wherein extra columns in the shape of misfit dislocations are visible along the  $[1\bar{1}0]$  and [001] crystallographic directions of CeO<sub>2</sub> thin film. After performing full relaxation, there was notable relaxation in atomic arrangement at the interface layer of CeO<sub>2</sub> and MgO, as well as at the surface layer of CeO<sub>2</sub>. The average equilibrium interfacial spacing between the film and the substrate is ~0.262 nm, with some neighboring atoms across the interface closer than this value and some slightly farther. For instance, at certain locations, the Mg – O bond length is 0.219 nm. Owing to electrostatic repulsion across the interface, cations and anions move away from cations and anions, respectively. Conversely, electrostatic attraction result in counterions moving closer to each other. Observed relaxation pattern is visible in Figure 1, wherein the side view shows the inward and outward movement of Ce, Mg, and O ions at the interface.

**Figure 2.** Top view (normal view) of interface atomic arrangement in the minimized  $CeO_2/MgO$  heterostructure shown in **Figure 1**. For clarity, only one atomic layer on each side of the minimized interface is shown for (a)  $CeO_2$  film (b) MgO substrate and (c)  $CeO_2/MgO$ . The geometrically optimized supercell is extended in the x and y directions (2 × 2) for better visualization, wherein  $CeO_2$  is above MgO. The black and blue boxed regions show the misfit dislocation network. The color scheme is same as in **Figure 1**.



To offer atomic scale details and a clearer view of the precise misfit dislocation structure, Figure 2 offers a normal view of the minimized interface with only one atomic layer shown on each side of the interface for CeO<sub>2</sub> and MgO. In Figure 2, the relaxed supercell is extended in x and y directions  $(2 \times 2)$  for better visualization. The misfit dislocation spacing is different in both the crystallographic directions because different number of columns are matched across the interface. A Burgers vector of  $a_{<100>}$  is projected along the CeO<sub>2</sub> [001] direction with misfit dislocation spacing of 1.65 nm (**Figure 2**). Along CeO<sub>2</sub>[1 $\overline{1}$ 0], a Burgers vector of  $\frac{a_{<110>}}{2}$  is estimated with the misfit dislocations split into partials that are separated by a stacking fault.<sup>80</sup> Each partial is repeated after 2.51 nm, but the two partials are separated by disparate distances due to mismatched unit cells. In Figure 2, the black boxed region consists of 4 unit cells of  $CeO_2[1\overline{1}0]$  matched with 3.5 unit cells of MgO[100], whereas 3 unit cells of  $CeO_2[1\overline{1}0]$  are matched with 2.5 unit cells of MgO[100] in the blue boxed region. As mentioned in the **Methodology**, 7 unit cells of  $CeO_2[1\overline{1}0]$  are matched with 6 unit cells of MgO[100] in total. The equilibrium atomic scale interface structure predicted from DFT is qualitatively comparable to the fully relaxed interface that we predicted using MD, 80 since it captures all possible nearestneighbor bonding scenarios. Clearly, the current treatment only modifies the misfit dislocation spacing along the  $[1\bar{1}0]$  direction in comparison to the fully relaxed case, but the fundamental properties of misfit dislocations are not expected to change. 91,92 It further validates our previous results obtained using MD, wherein we demonstrated that the rotation of the CeO2 thin film by 45° around the surface normal is one of the key mechanisms to remove surface dipole in CeO<sub>2</sub>/MgO heterostructures, <sup>80</sup> and explain the experimentally observed epitaxial relationship. <sup>71,75</sup> Herein, since the main goal is to understand oxygen vacancy formation and associated interface charge transfer, the present treatment will ensure a stable and tractable supercell for additional calculations. Notably, similar strategy has been used in the literature to study misfit dislocations using DFT and predict experimental behavior. 91,92 First principles-based atomic scale structure of CeO<sub>2</sub>/MgO interface and dissimilar misfit dislocation structure along the two crystallographic directions predicted in this work has not been reported in literature.

## 3.2 Oxygen vacancy formation at the interface

As oxygen vacancies are commonly encountered at oxide heterointerfaces<sup>93</sup> due to the processing conditions,<sup>67</sup> oxygen vacancy fraction is likely higher at misfit dislocations, which

will ultimately impact ionic conductivity. To increase the concentration of mobile ionic carriers, ceria-based thin film ionic conductors are often doped with lower valent elements leading to the formation of oxygen vacancies to maintain the defect equilibria. Consequently, understanding the formation and thermodynamic stability of oxygen vacancies at oxide heterointerfaces is imperative to design next-generation ionic conductors. Because we are mainly interested in studying the implications of oxygen vacancies on ionic conductivity at CeO<sub>2</sub>/MgO interfaces, we focus on calculating their formation energies in the interface layer of the CeO<sub>2</sub> thin film. Nonetheless, to offer comparison, we have computed oxygen vacancy formation at two different locations in the interface layer of the MgO substrate.

As described by the defect reaction given in **Equation 1**, substitution of two tetravalent cerium ions in ceria with trivalent dopant ions will result in formation of an oxygen vacancy at either 1NN, 2NN, or 3NN to the neighboring dopants. 42,43,44,52,57 In reality, at asymmetric and mismatched interface of CeO<sub>2</sub>/MgO, a multitude of distinct combinations are possible for the oxygen vacancy to be located next to two trivalent dopants. As shown in literature, although the influence of dopants could be extended to 3NN, 42,44 oxygen vacancy formation energies at 1NN and 2NN are lower in bulk ceria. In addition, our recent work using MD revealed that relative oxygen vacancies have preference to form at 1NN or 2NN or at a combination of these two distances near trivalent dopant at the CeO<sub>2</sub>/MgO interface.<sup>80</sup> The optimal position of dopant(s) is implicitly involved in this work. Since the introduction of dopants will spontaneously create oxygen vacancies to maintain defect equilibria, the results of vacancy preference will shed light on the dopant preference as well. In reality, there are a multitude of potential scenarios for the placement of Gd dopants, and as a result, diverse locations for the creation of oxygen vacancies are possible. However, owing to the extensive computational resources required to study defect formation in the present system, we strictly focus on handpicked configurations for oxygen vacancies at 1NN and 2NN to Gd dopants based on prior insights.<sup>80</sup>

However, among these select configurations, we have chosen diverse neighborhoods so as to cover dissimilar bonding scenarios at the interface. Gd is chosen as an illustrative case since it is one of the most widely used dopants in ceria-based ionic conductors. Although divalent doped ceria expected to yield higher fraction of oxygen vacancies, they are better suited for applications related to catalysis. Due to their widespread use in ceria-based ionic conductors for SOFC electrolyte applications, we have utilized gadolinium as the representative

case for trivalent dopants.<sup>36,42,44,46,48</sup> It is imperative to note that Gd-doped ceria exhibits higher ionic conductivity in IT-SOFCs as compared to other trivalent dopants.<sup>46</sup> Importantly, Gd-doped ceria thin films have been deposited on MgO substrates.<sup>74</sup> Besides, Gd can be contrasted with literature reports that focus on oxygen vacancy formation in bulk ceria. Since ionic radius of Gd<sup>3+</sup> (0.094 nm) is larger than host Ce<sup>4+</sup> (0.087 nm),<sup>94</sup> a higher fraction of Gd ions is expected to exist at the interface due to segregation.<sup>62</sup>

After peeling out a single atomic layer from either side of the interface (either CeO<sub>2</sub> or MgO layer), **Figure 3** depicts a normal view of the various locations used to create a vacancy in the interface layers. Numbers in **Figure 3** depict respective locations where oxygen vacancies were created. In Gd-doped ceria, each oxygen vacancy is created after adding two Gd<sup>3+</sup> dopants, as explained in **Methodology**. In each vacancy formation calculation, two Gd<sup>3+</sup> dopants are placed either in the interface layer (LI) of CeO<sub>2</sub> or the second layer (L2) of CeO<sub>2</sub> from the interface or in a combination of the two layers. That is, while the vacancies are chosen to form in the interface layer (LI), Gd dopants can be either in L1 or L2, which is necessary since the dopant-defect complex has numerous possible combinations. To clearly describe the vacancy locations, a simple naming scheme is utilized. For instance, in notation  $Ovac_{1NN,L1-2NN,L2}^{CeO2,3}$ , the superscript "CeO2,3" indicates that oxygen vacancy is in CeO<sub>2</sub> at location 3. The subscript "1NN,L1-2NN,L2" indicates that one Gd<sup>3+</sup> dopant is at 1NN to the vacancy in layer L1 and the other Gd<sup>3+</sup> dopant is at 2NN to the vacancy in layer L2. For reference, oxygen vacancy formation without the dopant is also computed at one location, which represents a simple case of oxygen vacancy formation in pure ceria, albeit at the heterointerface with MgO.

**Figure 3.** Locations (given by numbers) for oxygen vacancy formation at the interface layers of CeO<sub>2</sub> thin film and MgO substrate. Atomic color scheme is same as in **Figure 1**. In addition, red checkered and gold checkered spheres indicate possible oxygen vacancy locations in the CeO<sub>2</sub> thin film and MgO substrate, respectively. Green checkered spheres correspond to few possible locations for Gd dopant placement. For instance, with respect to the oxygen vacancy location **1**, two Gd dopants could be at 1NN or 2NN or a combination of those two sites. Blue line indicates the misfit dislocation network. Black dashed line shows the supercell boundary.

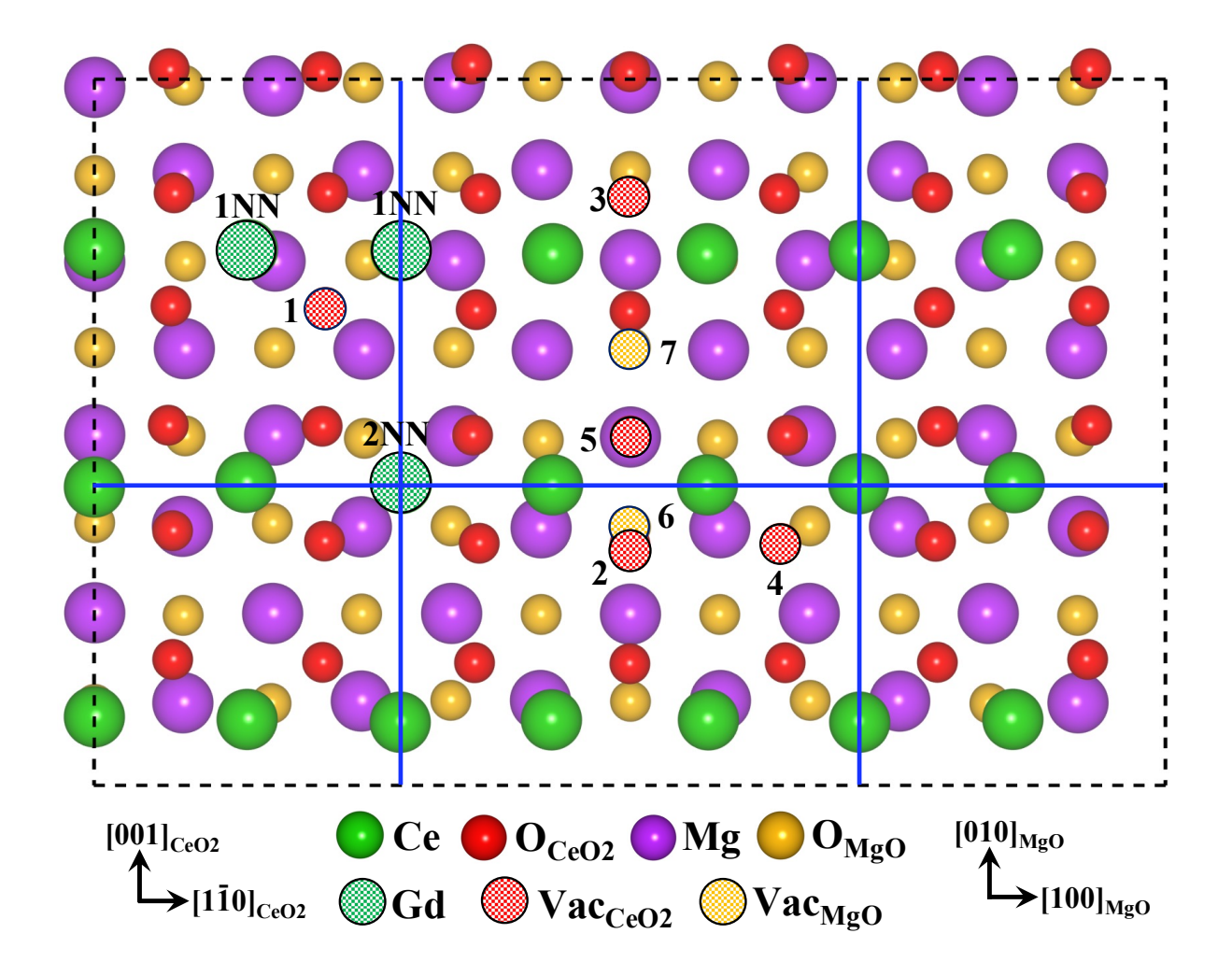


Table 1 offers oxygen vacancy formation energies for various locations at the interface as given in Figure 3. At the interface layer (*L1*) of CeO<sub>2</sub>, the vacancy formation energy in undoped ceria at *Ovac*<sup>CeO2,4</sup> is 1.071 eV. Because CeO<sub>2</sub> is a reducible oxide, this configuration is illustrative of a scenario in which oxygen vacancy is formed at the heterointerface due to reasons other than doping, such as experimental processing conditions.<sup>67</sup> Location 4 (Figure 3) is closer to the misfit dislocation, where an oxygen ion in CeO<sub>2</sub> is close to another oxygen in MgO across the interface. As a result, removing this oxygen is energetically preferred due to unfavorable electrostatic interaction. This is one of the likely reasons for lower oxygen vacancy formation energy (1.071 eV) at interfaces than values reported for bulk ceria<sup>42,43,52,95,96,97,98,99</sup> and low-index surfaces of ceria, <sup>95,96,100,101,102,103</sup> but falls within the range of values reported for edge dislocations in ceria, <sup>40</sup> which are not the same as misfit dislocations. <sup>76</sup> This result indicates that for given conditions, oxygen vacancy is thermodynamically favorable to form in the vicinity

of misfit dislocations at CeO<sub>2</sub>/MgO interface as compared to bulk ceria and ceria surfaces. **Figure S1** in the **Supporting Information** displays normal view of the relaxed interface layers after the introduction of the oxygen vacancy and Gd dopants for all the cases considered. In undoped ceria at *Ovac*<sup>CeO2,4</sup> (**Figure S1a**), the Ce ions close to the oxygen vacancy relax away from the vacancy, whereas the neighboring O ions relax toward the vacancy center. Analogous to bulk ceria, observed relaxation pattern is mainly due to electrostatic attraction and repulsion since the Ce ions move away from the vacancy since the ionized oxygen vacancy corresponds to a net effective positive charge, and the O ions move toward the vacancy. <sup>42,43</sup> As opposed to a single vacancy formation energy value in the bulk <sup>42,43,52,95,98</sup> and few dissimilar sites at the surfaces, <sup>101</sup> there are numerous distinct locations for oxygen vacancy formation in undoped CeO<sub>2</sub>/MgO interface, primarily due to the presence of misfit dislocations. Nonetheless, additional locations in undoped ceria have not been explored as our main focus is on studying the oxygen vacancy formation in Gd-doped CeO<sub>2</sub>/MgO heterostructure.

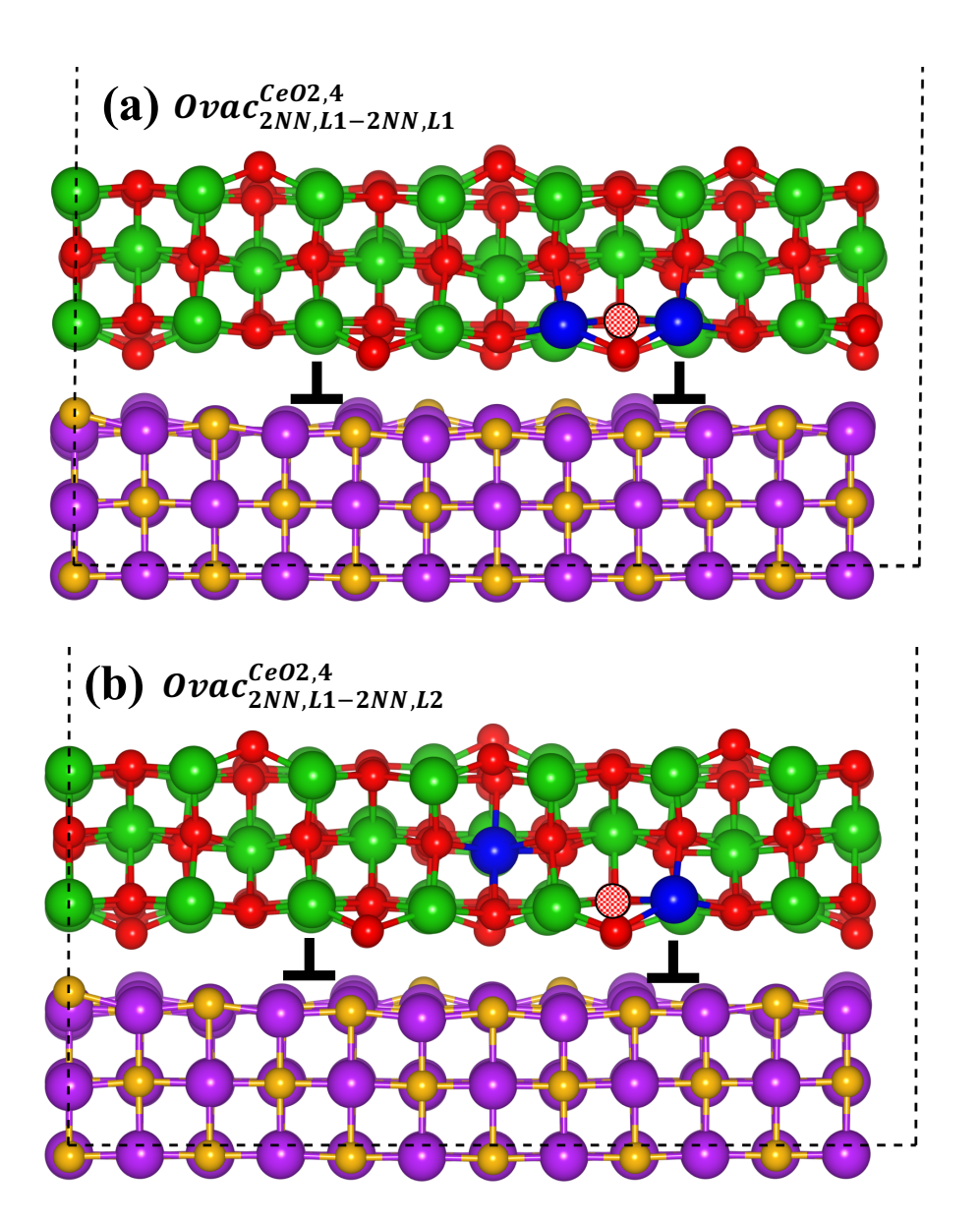
Formation energies for oxygen vacancy next to two trivalent Gd dopants for select few arrangements in the CeO<sub>2</sub> thin film range from -0.751 eV to 0.354 eV (Table 1). The entire range of energies is more favorable than undoped ceria. For two different dopant arrangements in layer L1,  $Ovac_{1NN,L1-2NN,L1}^{CeO2,1}$  and  $Ovac_{1NN,L1-1NN,L1}^{CeO2,1}$ , oxygen vacancy formation at location 1 exhibit positive formation energies of 0.354 eV and 0.168 eV, respectively. At this location (Figure 3), the oxygen vacancy in CeO<sub>2</sub> is essentially at the center of a square that has diagonally opposite Mg ions and O ions across the interface. Oxygen vacancy at location 1 prefers 1NN-1NN with one dopant on the dislocation line and the other not on it as compared to 1NN-2NN, where both dopants are on the dislocation line. The local electrostatic balance across the interface is effectively maintained, resulting in positive formation energy for anion removal. This is in contrast with oxygen vacancy formation in the bulk of Gd-doped ceria, where similar dopant-defect arrangements exhibit negative formation energies since doping with trivalent ions lead to spontaneous vacancy formation as governed by the defect equilibria. 42,44 SI Figure 1b and 1c show the atomic relaxation pattern, where the neighboring O ions relax toward the vacancy, whereas the larger Gd dopants and neighboring Ce ions move away from the vacancy center, which is consistent with that observed in bulk ceria. Across the interface, this electrostatic interaction results in movement of Mg ions away from the vacancy and O ions in MgO relax toward the vacancy, but the net movement is less pronounced.

**Table 1.** Oxygen vacancy formation energies  $(E_f)$  at the interface layer of the CeO<sub>2</sub>/MgO heterostructure. The corresponding vacancy locations are shown in **Figure 3**. The nomenclature for vacancy location with respect to dopants is explained in the main text. For various defect configurations, the induced electron transfer  $(\Delta n_e)$  from MgO to CeO<sub>2</sub> is also provided.

Vacancy location	$E_f$ (eV)	$\Delta n_e(e)$	Vacancy location	$E_f$ (eV)	$\Delta n_e(e)$
Ovac <sup>CeO2,4</sup>	1.071	1.78	$Ovac^{CeO2,4}_{2NN,L1-2NN,L2}$	-0.437	1.83
$Ovac^{CeO2,1}_{1NN,L1-2NN,L1}$	0.354	1.72	$Ovac^{CeO2,4}_{2NN,L1-2NN,L1}$	-0.625	1.76
$Ovac^{CeO2,1}_{1NN,L1-1NN,L1}$	0.168	1.75	$Ovac^{CeO2,4}_{1NN,L1-1NN,L1}$	-0.751	1.79
$Ovac^{CeO2,2}_{1NN,L1-2NN,L1}$	-0.283	1.81	$Ovac^{CeO2,4}_{1NN,L1-2NN,L1}$	-0.415	1.72
$Ovac^{CeO2,2}_{1NN,L1-1NN,L1}$	-0.179	1.79	$Ovac^{CeO2,5}_{1NN,L1-1NN,L1}$	0.338	1.70
$Ovac^{CeO2,3}_{1NN,L1-2NN,L2}$	-0.364	1.59	$Ovac^{Mg0,6}_{iNN,L1-iNN,L1}$	1.129	1.52
$Ovac^{CeO2,3}_{1NN,L1-1NN,L2}$	-0.446	1.64	$Ovac_{2NN,L1-2NN,L1}^{MgO,7}$	2.581	1.38

As opposed to endothermic oxygen vacancy formation energies at location 1, at location 2 (**Figure 3**),  $Ovac_{1NN,L1-2NN,L1}^{CeO2,2}$  and  $Ovac_{1NN,L1-1NN,L1}^{CeO2,2}$  eV and -0.179 eV, respectively. With both the dopants in layer LI, 1NN–2NN is energetically preferred over 1NN–1NN, which is reverse to the preference observed at location 1. At location 2, 1NN–1NN has both the dopants on the dislocation line, whereas in 1NN-2NN, the dopant at 1NN is on the dislocation line but the one at 2NN is not. Oxygen vacancy in CeO<sub>2</sub> at location 2 is sitting above another oxygen in MgO, which creates chemical frustration due to unfavorable electrostatic interactions. As a result, removal of an oxygen ion from this location is exothermic regardless of the dopant arrangement, 80 an outcome also reported for other oxide heterointerfaces. Although the overall structural relaxation is similar to the oxygen vacancy at location 1, an adjacent O ion in CeO<sub>2</sub> undergoes noticeable relaxation toward the vacancy center at location 2, which is evident in **SI Figure 1d** and **1e**.

**Figure 4.** Side view of  $CeO_2/MgO$  heterostructure obtained after full energy minimization and geometry optimization for configurations (a)  $Ovac_{2NN,L1-2NN,L1}^{CeO_2,4}$  and (b)  $Ovac_{2NN,L1-2NN,L2}^{CeO_2,4}$ . Atomic color scheme and interface orientation relationship are same as in **Figure 1**. Blue and red checkered spheres respectively correspond to Gd dopants and oxygen vacancies.



So far, at vacancy locations 1 and 2, both the dopants have been placed in layer L1 of  $CeO_2$  to study their impact on oxygen vacancy formation at the interface. Furthermore, either one or both the dopants were placed on the dislocation line to assess the impact of misfit dislocations. However, it is likely that one of the dopants is located in layer L2 and that neither of the dopants

are on the dislocation line. To investigate this possible scenario, oxygen vacancy is created above another oxygen in MgO at location 3 (**Figure 3**) for two configurations  $Ovac_{1NN,L1-2NN,L2}^{CeO2,3}$  and  $Ovac_{1NN,L1-1NN,L2}^{CeO2,3}$ , which yield exothermic formation energies of -0.364 eV and -0.446 eV, respectively. In these configurations with one dopant in L1 and another in L2, 1NN-1NN is energetically preferred over 1NN-2NN. The energetic preference of 1NN-1NN is in contrast to that observed in bulk CeO<sub>2</sub>, wherein the vacancy formation energy is lower with the dopants in 1NN-2NN configuration. <sup>42,44,52</sup> A potential explanation for this trend is that since both the dopants are in different layers, the structural relaxation due to oxygen vacancy formation and insertion of larger trivalent dopants is accommodated within individual layers L1 and L2. In both cases, (**SI Figure 1f** and **1g**) oxygen ion in CeO<sub>2</sub> located near the oxygen vacancy relaxes toward the Mg ion due to Coulombic attraction. Similar to location 2, chemical frustration arising due to anion-anion interaction is one of the primary reasons for exothermic formation energies at location 3.

We have not yet examined configurations having both dopants at 2NN. To address this scenario, vacancy location 4 (Figure 3) was studied for four configurations having dopants at 1NN, 2NN, and a combination of these two distances with at least one dopant on the dislocation line. Given in Table 1, oxygen vacancy formation energies for the four configurations  $Ovac_{2NN,L1-2NN,L1}^{CeO2,4},\ Ovac_{2NN,L1-2NN,L2}^{CeO2,4},\ Ovac_{1NN,L1-1NN,L1}^{CeO2,4},\ \text{and}\ Ovac_{1NN,L1-2NN,L1}^{CeO2,4}\ \text{are}\ \ \text{-}0.625$ eV, -0.437 eV, -0.751 eV, and -0.415 eV respectively, implying their spontaneous formation. Since location 4 is one of the most favorable location for vacancy formation, side view of the relaxed geometries for two configurations are given in Figure 4 to offer clarity in the relaxation pattern due to dopant in layers L1 and L2. Configurations with both dopants in layer L1 are more favorable than one where one of the dopants is in layer L2, indicating that larger trivalent dopants are better accommodated at the interface layer. This strategy of fixing the vacancy at location 4 and altering various possible positions of Gd dopants allows for the prediction of lowest energy configuration and shed light on the ordering rules for impurities at misfit dislocations. The most favorable configuration is when both dopants are at 1NN to the oxygen vacancy, which is in slight contrast to that observed in bulk ceria. 42,44,52 Corresponding top view of the relaxed interface layers after vacancy formation at location 4 is offered in SI Figure 1h, 1i, 1j, and 1K. Noticeable relaxation of neighboring oxygen ions in CeO<sub>2</sub> toward the vacancy center and larger cations (Gd and neighboring Ce) moving away from the vacancy center is

observed, which is qualitatively similar to the relaxation pattern observed at vacancy locations 2 and 3.

Oxygen vacancy location 2, 3, and 4 (**Figure 3**) exhibit exothermic formation energies since they are created in a region of unfavorable electrostatic interaction, *i.e.*, anion–anion neighborhood across the interface. On the contrary, oxygen vacancy at location 1 exhibit endothermic formation energies owing to their creation at favorable electrostatic interaction, *i.e.*, anion–cation neighborhood across the interface. To further study the latter situation, but at a different locality, oxygen vacancy at location 5 (**Figure 3**) was created by removing an oxygen ion in CeO<sub>2</sub> that sits above neighboring Mg ion across the interface. Oxygen vacancy formation energy for configuration  $Ovac_{1NN,L1-1NN,L1}^{CeO2,5}$  was found to be 0.338 eV, wherein both dopants located on the dislocation line are at 1NN to the vacancy. This result reveals that oxygen vacancies are thermodynamically less likely to occur at locations that have anion–cation interaction across the interface, even if the dopants are located on the dislocation. The relaxation pattern in **SI Figure 11** display that the neighboring oxygen ion moves toward the vacancy center. However, since the new location is right above another oxygen ion in MgO, this relaxing oxygen is pulled inwards *i.e.*, away from the interface.

Although we have studied several distinct oxygen vacancy locations in Gd-doped CeO<sub>2</sub>, oxygen vacancies could occur on the MgO side of the interface since the dopants are most likely to exist at the interface layer LI due to segregation. In order to explore this possibility, we studied oxygen vacancy formation at location 6 and 7 (Figure 3) in MgO via configurations  $Ovac_{NN,L1-iNN,L1}^{MgO,6}$  and  $Ovac_{NN,L1-2NN,L1}^{MgO,7}$ . In these two configurations, Gd dopants are located at the interface layer (LI) of CeO<sub>2</sub>, with the NN distances representing those typically encountered in CeO<sub>2</sub>. As a result, at location 6, both dopants at iNN indicates that the distance is intermediate of 1NN and 2NN ( $\sim$ 0.33 nm), whereas for location 7, both dopants are at 2NN. Configuration  $Ovac_{iNN,L1-iNN,L1}^{MgO,6}$  (SI Figure 1m), where both dopants are located on the dislocation line and oxygen vacancy in MgO sits below another oxygen ion in CeO<sub>2</sub>, exhibits endothermic formation energy of 1.129 eV. It is imperative to note that this configuration is precisely opposite of  $Ovac_{1NN,L1-1NN,L1}^{CeO_{2,2}}$  in that the oxygen vacancy is created on the opposite side of the interface with dopants at the same location. Vacancy formation energy for configuration  $Ovac_{2NN,L1-2NN,L1}^{MgO,7}$  (SI Figure 1n) is 2.581 eV, where neither of the dopants are on the

dislocation line, and oxygen vacancy in MgO sits below another oxygen ion in CeO<sub>2</sub>, but only slightly farther than the previous case. In these two scenarios, contrasting to the outcome for oxygen vacancy formation in CeO<sub>2</sub>, removal of an oxygen ion from electrostatically unfavorable interface region (anion–anion) is not exothermic, further revealing that oxygen vacancy formation is sensitive not only to the local electrostatic environment, but also on the material in consideration. In both cases, after oxygen vacancy formation in MgO, neighboring Mg ions relax away and oxygen ions relax toward the vacancy center (SI Figure 1m and 1n), a relaxation pattern qualitatively similar to that observed for oxygen vacancy in CeO<sub>2</sub>.

Oxygen vacancy formation energies in MgO are significantly higher than those in CeO<sub>2</sub> for comparable neighboring environment, indicating that at the interfaces of Gd-doped CeO<sub>2</sub>/MgO heterostructures, oxygen vacancies are most likely to be encountered in CeO<sub>2</sub>. Because the present calculations are conducted at 0 K, exothermic formation energies for several different locations in CeO<sub>2</sub> thin film indicate that CeO<sub>2</sub>/MgO interfaces will undoubtedly have higher concentration of oxygen vacancies. In addition, little increase in temperature could lead to facile formation of oxygen vacancies at few other interface locations. In bulk Gd-doped ceria, vacancy formation is lowest when one dopant is at 1NN and the other at 2NN.<sup>42,44,52</sup> Calorimetric measurements also report a similar preference of oxygen vacancies to remain at 1NN to Gd in bulk ceria.<sup>104</sup> In slight contrast, at CeO<sub>2</sub>/MgO interface, the most favorable arrangement has both the dopants at 1NN (*Ovac*<sup>CeO2,4</sup><sub>1NN,L1-1NN,L1</sub>). In the latter case, misfit dislocations have a huge impact on vacancy formation energies. For instance, for a given dopant arrangement, disparate vacancy formation energies at the interface are probable, specifically in the vicinity of misfit dislocations, whereas a single value for formation energy is expected in the bulk.

In general, the addition of Gd dopants influences the local atomic relaxation and increases the lattice constant slightly due to its larger ionic radius as compared to the host Ce ion. For doped heterostructures, this influences the lattice mismatch, but only marginally as the dopant concentration is very small. As compared to bulk ceria, large spread in oxygen vacancy formation energies is witnessed at misfit dislocations in CeO<sub>2</sub>/MgO heterostructures. As such, most interfaces are hypothesized to facilitate facile formation of oxygen vacancies. However, as demonstrated here, certain locations at CeO<sub>2</sub>/MgO interface are not conducive for oxygen vacancies, while some neighborhoods thermodynamically favor vacancy formation. This could really complicate the landscape at misfit dislocations, especially since greater fraction of dopants

are expected to dwell at interfaces due to segregation. In this scenario, there would be regions at the interface having dopants but lack of mobile carriers, which could influence ionic conductivity. This could be one of the possible reasons for contradictory outcomes reviewed in Introduction, where several experiments report enhanced ionic conductivity at misfit dislocations, 6,7,8,15,16,17,18,19,20,21 while some experiments observe no obvious influence of misfit dislocations. <sup>22,23,38,39,40,41</sup> However, additional factors<sup>80</sup> contributing to the inconsistent behavior in ionic transport are not well understood and requires further investigation via dynamic modeling of defect diffusion in the neighborhood of dopants. It is plausible that the actual scenario is way more complex at oxide heterointerfaces, where factors such as temperature, strain, oxygen partial pressure, and dopant segregation could potentially influence the vacancy dynamics. In addition, present calculations are conducted for dilute concentration of dopants and defects. At higher concentration, formation of one oxygen vacancy is likely to impact the formation energies of additional vacancies in the neighborhood owing to vacancy-vacancy interactions. Although calculations addressing such complexity are beyond the scope of this work, current results make a compelling case to pursue them in future work. In general, present results shed light on the complexity faced at oxide heterointerfaces, further revealing that studying oxygen vacancy formation at misfit dislocations is the most fundamental prerequisite to identify ionic transport mechanisms at interfaces.

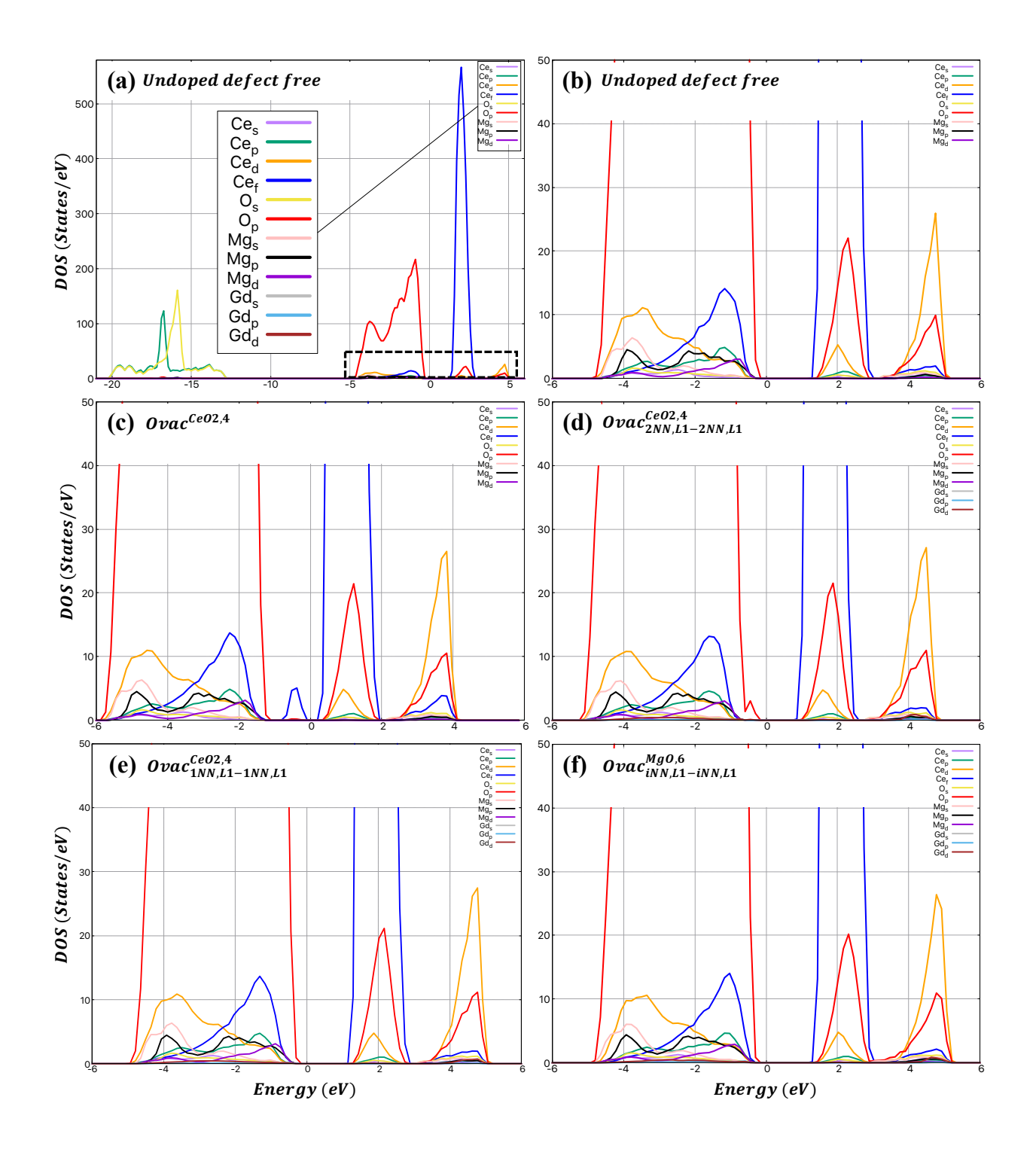
## 3.3 Electronic structure of the interface

Detailed density of states (DOS) analysis was performed to gain insights into the electronic structure of the interface with and without the defects. By comparing DOS before and after inclusion of oxygen vacancies and corresponding dopants, modifications in the electronic states can be visualized near the Fermi level. As shown in **Figure 5**, DOS were projected on the Ce, O, Mg, and Gd ions and their respective orbitals. Fermi level is set to 0 eV, so states with negative and positive energies indicate occupied and unoccupied (virtual) orbitals, respectively. **Figure 5a** portrays DOS for the minimized clean (undoped defect free) heterostructure, wherein the low-lying Ce 5s states around -34 eV have been omitted. Region between -13 eV to -20 eV mainly comprises of Ce 5p and O 2s states. In order to focus on DOS at and around the Fermi level, **Figure 5b** shows amplification of the boxed region in **Figure 5a**. The valence band in CeO<sub>2</sub>/MgO heterostructure predominantly comprises of O 2p orbitals with contributions from Ce 5d and 4f orbitals, as well as minor contributions from Mg 2p, 3s, 3d and Ce 5p orbitals. The

conduction band primarily contains Ce 4*f* orbitals along with noticeable presence of O 2*p* and Ce 5*d*, as well as very small contributions from Ce 5*p*, Mg 2*p*, and Mg 3*s* orbitals. The overlap of orbital signatures from various elements in the valence band reveal strong interfacial chemical bonding. The valence band and conduction band in CeO<sub>2</sub>/MgO heterostructure is dominated by Ce and O orbitals. Calculated value for the gap between O 2*p* and Ce 4*f* states is 1.44 eV, which is smaller than the gap of 2.06 eV reported for bulk CeO<sub>2</sub> using similar methodology. <sup>43</sup> However, it is imperative to note that bulk CeO<sub>2</sub> and CeO<sub>2</sub>/MgO heterostructure cannot be compared on the same basis, since the latter has misfit dislocations and associated interface strain. Moreover, the complex interface atomic environment comprising of Ce, Mg, and O ions (from both fluorite and rocksalt phases) leading to interfacial chemical bonding is likely to influence this behavior.

For clarity in DOS analysis of defective heterostructures, amplified region close to the Fermi level is only displayed, which is given by the boxed region in **Figure 5a**. DOS for oxygen vacancy in undoped ceria at *Ovac*<sup>CeO2,4</sup> is displayed in **Figure 5c**. In reduced ceria, a new peak comprising predominantly of Ce 4f states emerges between the top of the valence band and the bottom of the conduction band, whereas the Fermi level is now positioned in the gap between this new peak and the unoccupied Ce 4f states. Emergence of the new Ce 4f peak in the gap, often known as metal-induced gap states (MIGS), is consistent with reported results for reduced ceria, wherein introduction of an oxygen vacancy result in two excess electrons, which localize on the Ce 4f orbitals. 43,95,97,98,101 Bader charge analysis confirmed that the Ce 4f electrons are completely localized on two Ce ions near the oxygen vacancy, resulting in reduction of Ce atoms and the emergence of gap states. Except the new peak in gap states, the qualitative signatures and composition of valence and conduction bands are more or less similar to that observed in the undoped defect free CeO<sub>2</sub>/MgO heterostructure (**Figure 5b**).

**Figure 5.** For CeO<sub>2</sub>/MgO heterostructures, electronic density of states (DOS) projected onto Ce, O, Mg, and Gd atoms in (a) Undoped defect free. Magnified boxed region in (a) for (b) Undoped defect free (c)  $Ovac^{CeO_2,4}$  (d)  $Ovac^{CeO_2,4}_{2NN,L1-2NN,L1}$  (e)  $Ovac^{CeO_2,4}_{1NN,L1-1NN,L1}$  (f)  $Ovac^{MgO,6}_{iNN,L1-iNN,L1}$ . In order to focus on the DOS features around the Fermi level, low-lying states are not shown. Only spin-up channel is shown as spin-down channel is almost identical. In all cases, the Fermi level is shifted to 0 eV. A magnified panel for labels of projected orbitals is given in (a).



DOS for two of the most favorable oxygen vacancy location  $Ovac_{2NN,L1-2NN,L1}^{CeO2,4}$  and  $Ovac_{1NN,L1-1NN,L1}^{CeO2,4}$  is given in **Figure 5d** and **5e**, respectively. In these configurations since two trivalent Gd dopants are introduced along with an oxygen vacancy, the localized gap states visible in reduced ceria (**Figure 5c**) disappear because of charge compensation, which has been

reported in literature for doped ceria<sup>102</sup> as well as surfaces of Gd-doped ceria.<sup>105</sup> As a result, the two electrons left behind due to inclusion of oxygen vacancy do not localize on Ce 4f orbitals. However, even in doped CeO<sub>2</sub>, gap states are likely to emerge analogous to that observed in undoped reduced ceria. 96,98,100 The gap between O 2p and Ce 4f states for  $Ovac_{2NN,L1-2NN,L1}^{CeO2,4}$ (Figure 5d) is decreased as compared to the undoped defect free (Figure 5b) and  $Ovac_{1NN,L1-1NN,L1}^{CeO2,4}$  (Figure 5e) case since the conduction band moves closer to the Fermi level, but qualitative signatures of various orbitals in the valence and conduction band are unaffected. Similar electronic structure of the interface is uncovered for other configurations with two Gd dopants and an oxygen vacancy. Figure 5f displays the DOS for  $Ovac_{iNN,L1-iNN,L1}^{Mg0,6}$ . Evidently, as compared to the undoped defect free case, the overall qualitative features in the DOS are unaltered regardless of the oxygen vacancy location in either CeO<sub>2</sub> (Figure 5d and 5e) or in MgO (Figure 5f). Analysis of DOS for other vacancy locations (Figure 3) revealed that the qualitative signatures of occupied and virtual orbitals is analogous to that given in Figure 5e and **5f.** For instance, DOS for  $Ovac_{1NN,L1-2NN,L1}^{CeO2,2}$ ,  $Ovac_{2NN,L1-2NN,L2}^{CeO2,4}$ , and  $Ovac_{1NN,L1-1NN,L2}^{CeO2,3}$  are given in SI Figure S2. In comparison to  $Ovac_{2NN,L1-2NN,L1}^{CeO2,4}$  (Figure 5d), the gap between O 2pand Ce 4f states is larger for rest of the configurations. In general, it can be concluded that charge compensation via inclusion of two Gd dopants with an oxygen vacancy result in comparable electronic structure of the Gd-doped CeO<sub>2</sub>/MgO heterostructure as long as the two dopants are at 1NN or 2NN or combination of these distances near the oxygen vacancy. On the contrary, the electronic structure of the undoped heterostructure with a vacancy defect is noticeably different due to the appearance of gap states.

## 3.4 Electronic charge transfer at the interface

To estimate the interfacial interaction as well as comprehend the charge redistribution and interface charge transfer between  $CeO_2$  and MgO, charge density differences before and after the charge transfer were computed. The charge density difference ( $\Delta\rho$ ) was computed using

$$\Delta \rho = \rho_{(CeO2/MgO)} - \rho_{(CeO2)} - \rho_{(MgO)} \tag{3}$$

where  $\rho_{(CeO_2/MgO)}$ ,  $\rho_{(CeO_2)}$ , and  $\rho_{(MgO)}$  correspond to the charge density of the CeO<sub>2</sub>/MgO heterostructure, isolated CeO<sub>2</sub>, and isolated MgO, respectively. Hence,  $\Delta \rho$  demonstrates the

charge density variations in CeO<sub>2</sub> and MgO when they are brought in contact. When computing  $\Delta \rho$  for the heterostructure with dopants and defects, various terms in **Equation 3** were modified accordingly. For the undoped defect free CeO<sub>2</sub>/MgO heterostructure, Figure 6a depicts the x-y plane-averaged charge density difference along the z-direction, whereas **Figure 6b** (side view) and 6c (top view) show the 3D difference charge density plots. It is clear to see that the charge transfer predominantly occurs at the interface. In the vicinity of the interface, plane-averaged charge density difference  $\Delta \rho(z) > 0$  for CeO<sub>2</sub> layer and  $\Delta \rho(z) < 0$  for MgO layer (**Figure 6a**). However, precisely at the interface (Figure 6a), both the CeO<sub>2</sub> and MgO layers appear to lose some charge, which is accumulated at the interface between the two layers and cannot be attributed to either of them. It is imperative to note that the difference in isosurfaces between CeO<sub>2</sub> and MgO is very small. Closer inspection of the 3D isosurfaces (Figure 6b and 6c) indicate that CeO<sub>2</sub> has slightly more positive isosurfaces as compared to MgO layer, and the charge transfer mechanism occurs via CeO<sub>2</sub> layer gaining a small amount of charge whereas MgO layer does the opposite. In regions of oppositely charged species linked across the interface, the ionic character of the interface bonding is apparent. An interesting aspect to note is that asymmetry, disparate bond lengths, and presence of misfit dislocations at the interface lead to the charges being distributed asymmetrically. For instance, charge transfer is more pronounced in few areas closer to misfit dislocations and neighborhoods that have shorter bond lengths across the interface.

To elucidate the influence of oxygen vacancies and Gd dopants on the electronic charge transfer across the interface, **Figure 7** displays 3D difference charge density plots for few select configurations. Similar to undoped defect free heterostructure, closer inspection of the difference charge density plot for oxygen vacancy location  $Ovac_{2NN,L1-2NN,L1}^{CeO2,4}$  (**Figure 7a**) illustrates that charge transfer occurs from MgO to CeO<sub>2</sub>. Region closer to the two Gd dopants that are at 2NN to the oxygen vacancy lose slight charge, whereas the oxygen ion bonded to the two Gd dopants and the two Ce ions on the dislocation line located at 1NN to the oxygen vacancy gain some charge. Even in this case, charge transfer is more prominent in the vicinity of misfit dislocations. For the configuration  $Ovac_{1NN,L1-2NN,L2}^{CeO2,3}$ , the difference charge densify profile (**Figure 7b**) is somewhat altered. In this configuration, both Gd dopants and oxygen vacancy are far from the dislocation, as well as one Gd dopant is in layer L2, which influences the ensuing dissimilar charge distribution. The charge transfer nevertheless happens from MgO to CeO<sub>2</sub>. Regions close

to Ce atoms on the dislocations lines mostly gain charge. The area closer to oxygen vacancy and Gd dopants results in a complex accumulation-depletion zone.

**Figure 6.** Electronic charge transfer across undoped defect free CeO<sub>2</sub>/MgO heterostructure. (a) x-y plane-averaged charge density difference  $\Delta \rho(z)$  along the z-direction. Three-dimensional charge density difference plots for (b) Side view and (c) Top view. Only interface layer atoms on each side of the interface are shown. Green, purple, and red spheres correspond to Ce, Mg, and O ions, respectively. Yellow and cyan isosurfaces indicate regions of charge accumulation and depletion, respectively. The isosurface value is  $1.1 \times 10^{-3} \, e/\text{Å}^3$ . Blue lines in (c) show the misfit dislocation network.

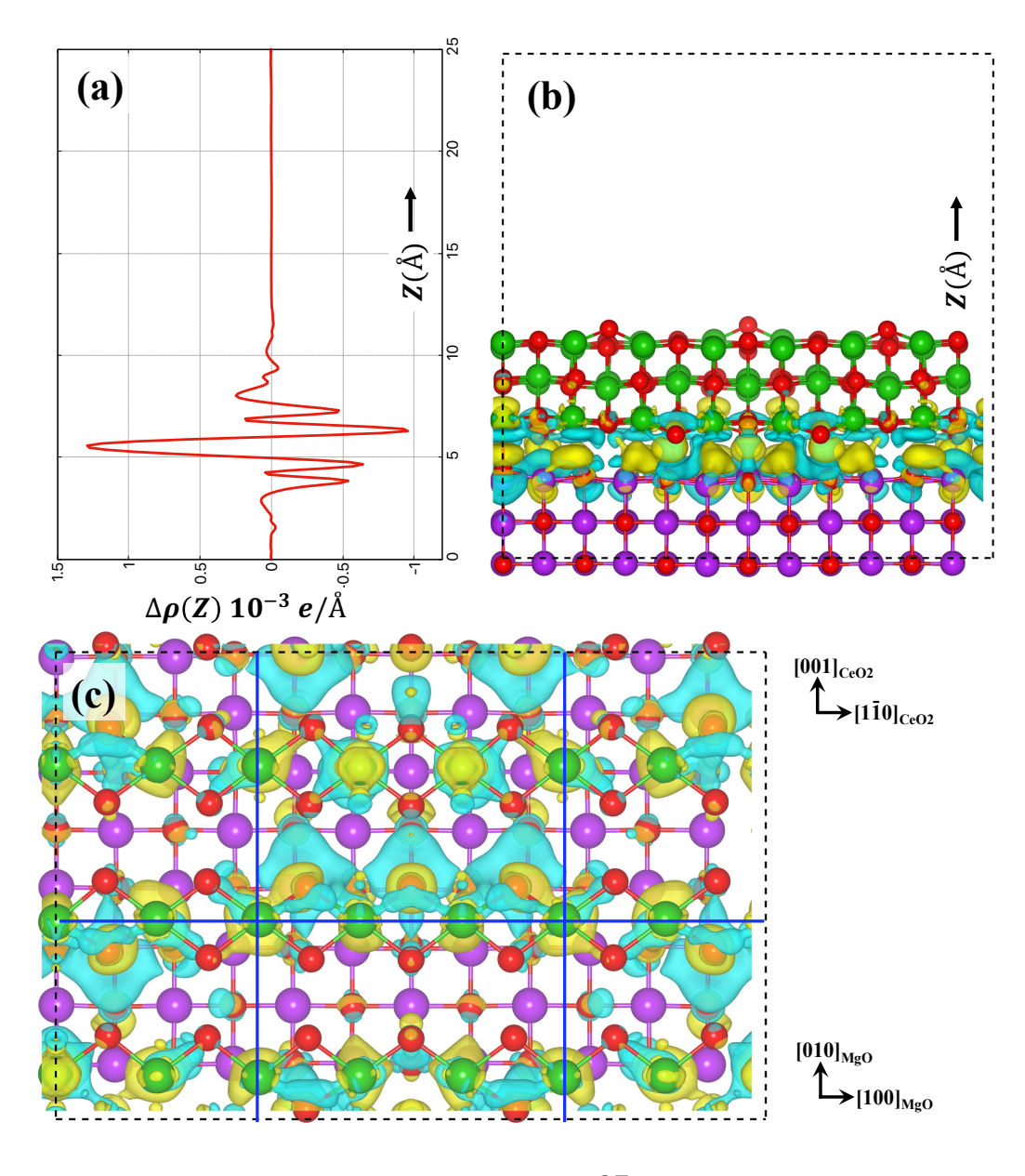
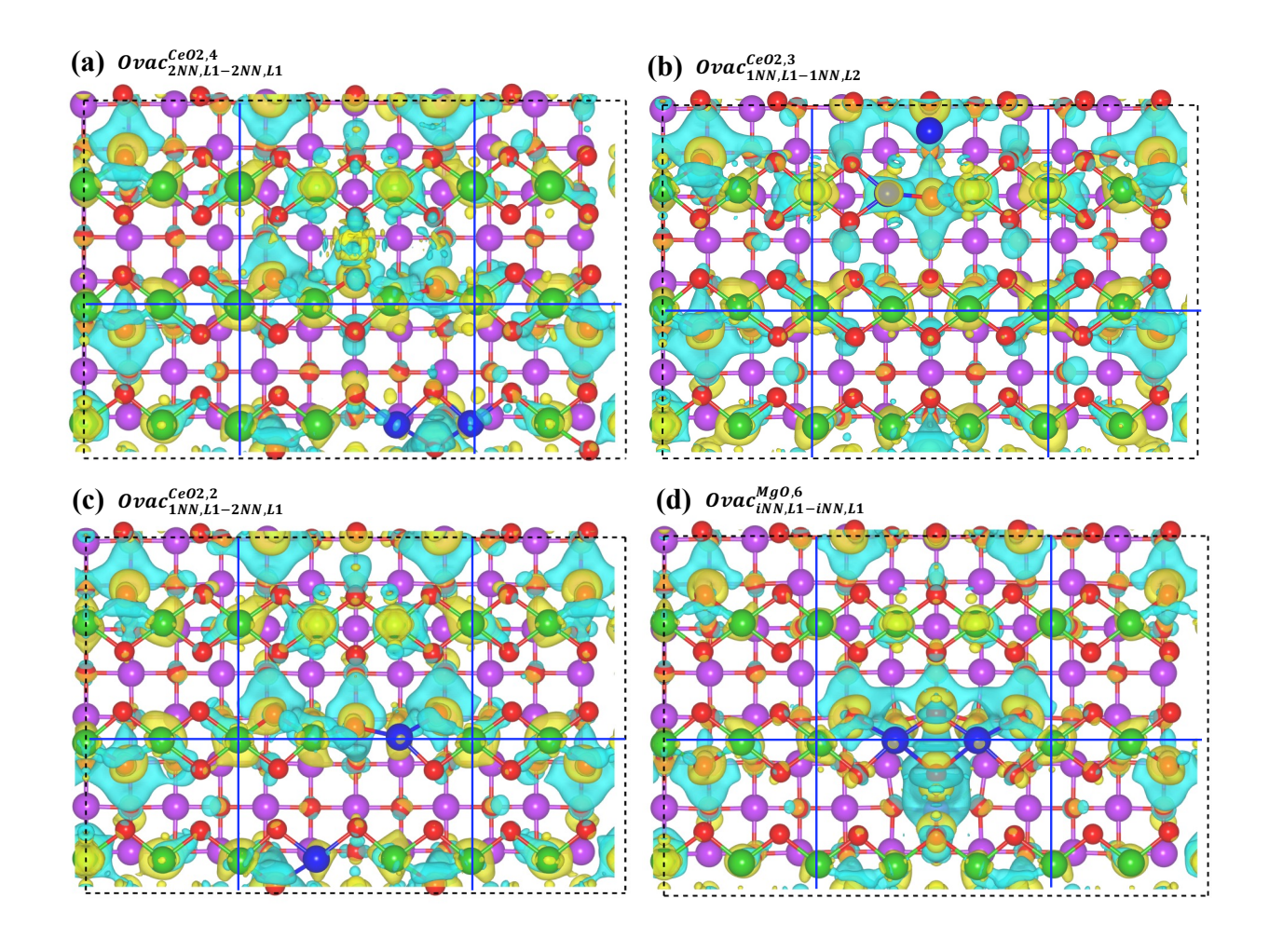


**Figure 7.** Top view of three-dimensional charge density difference plots for configurations (a)  $Ovac_{2NN,L1-2NN,L1}^{CeO2,4}$  (b)  $Ovac_{1NN,L1-1NN,L2}^{CeO2,3}$  (c)  $Ovac_{1NN,L1-2NN,L1}^{CeO2,2}$  and (d)  $Ovac_{iNN,L1-iNN,L1}^{MgO,6}$ . Only interface layer atoms are shown. Blue spheres correspond to Gd ions. Rest of the color scheme is same as in **Figure 6**.



To elucidate a slightly different scenario, difference charge density for configuration  $Ovac_{1NN,L1-2NN,L1}^{CeO2,2}$  was studied (**Figure 7c**), wherein one of the Gd dopants is on the dislocation and the oxygen vacancy is very close to the dislocation line. Region close to Ce atoms on the dislocation gain charge, whereas MgO loses charge. However, some regions close to the interface do fluctuate somewhat. Area close to the two Gd dopants lose very little charge. So far, interface charge transfer after oxygen vacancy formation in CeO<sub>2</sub> has been considered. In order to visualize the difference charge density after oxygen vacancy is introduced in MgO,

configuration  $Ovac_{iNN,L1-iNN,L1}^{Mg0,6}$  was examined (**Figure 7d**). Even in this scenario, Ce atoms gain charge, but this accumulation is more pronounced for Ce atoms located on the dislocation. The two Gd dopants on the dislocation are not affected much and exhibit very minor loss of charge. The direction of charge transfer from MgO to CeO<sub>2</sub> is analogous to previous cases. In this case, the region surrounding the oxygen vacancy in MgO lose substantial charge, which is evident in **Figure 7d**. The only difference between  $Ovac_{1NN,L1-2NN,L1}^{CeO2,2}$  and  $Ovac_{iNN,L1-iNN,L1}^{Mg0,6}$  is that the vacancy is on either side of the interface (**Figure 3**) since this region contains two oxygen ions in close vicinity across the interface. Removing either oxygen result in different charge accumulation and depletion pattern close to the vacancy, but region far from it exhibit similar features (**Figure 7c** and **7d**). In general, the intricate accumulation and depletion regions vary along the interface for all cases, wherein a common trend of charge transfer from MgO to CeO<sub>2</sub> is witnessed, predominantly in the interfacial region. Similar to the undoped defect free case (**Figure 6**), a closer examination of the charge density difference for various vacancy configurations (**Figure 7**) demonstrates a small amount of charge transfer from MgO to CeO<sub>2</sub>.

Electronic distribution and charge transfer at oxide interfaces has fundamental influence on material behavior. To support the results for mechanism of charge transfer and to gain deeper insights into the interlayer charge transfer, we further performed quantitative analysis based on Bader charges, 106,107 which offers basic information pertaining to charges on atoms and as a result shed light on the charge transfer between interfacial atoms of different species. Using bulk references for CeO<sub>2</sub> and MgO, atomic electron transfer among atoms on both side of the interface are computed from net Bader charges. For the undoped defect free CeO2/MgO heterostructure, a net electronic charge of 1.85e per supercell is transferred from MgO to CeO<sub>2</sub>. The observed charge transfer is mainly attributed to oxygen ions in MgO losing charge, whereas cerium ions gaining charge, an effect that is more prominent in interface layer cerium ions. For instance, interface oxygen ions in MgO lose  $\sim 0.04 - 0.06e$ , whereas interface cerium ions gain  $\sim 0.05 - 0.07e$ , which results in cerium ions being partially reduced from  $Ce^{4+}$  to  $Ce^{\delta+}$  with  $\delta$ ranging from 3.93 - 3.95. Since none of the cerium ions are fully reduced to  $Ce^{3+}$ , the observed charge transfer is qualitatively supported by DOS (Figure 5b), which does not reveal cerium 4f peak in the gap states. On the contrary, the cerium 4f peak is clearly visible in DOS (Figure 5c) for Ovac<sup>CeO2,4</sup> because in this case, two cerium ions neighboring the oxygen vacancy are reduced to  $Ce^{3+}$ .

Similarly, Bader charge analysis (Table 1) was performed for all the vacancy configurations, which reveal a common trend of charge transfer from MgO to CeO<sub>2</sub>. For all the vacancy locations, the charge transfer from MgO to CeO<sub>2</sub> ranges from 1.52e - 1.83e per supercell, which is slightly less as compared to undoped defect free heterostructure. In all cases, interface layer atoms undergo the most noticeable change in Bader charges revealing the influence of misfit dislocations. A clear trend correlating the location and stability of vacancies with the net magnitude of electronic charge transfer is not obvious. Nonetheless, the lowest amount of electronic charge transfer is observed for the two oxygen vacancy locations in MgO, which are also energetically least favorable. Overall, the Bader charge analysis supports the results of charge density difference, confirming the charge transfer mechanism from MgO to CeO<sub>2</sub>. Misfit dislocations play a crucial role in the interface charge transfer mechanism since accumulation and depletion zones (Figure 7) and Bader charges (Table 1) are prominent in their vicinity. As a result, interface charge transfer is expected to govern the stability of misfit dislocations as well as the heterostructure. In addition, interface electronic charge transfer will influence the formation of oxygen vacancies, which will ultimately impact the ionic transport in thin film oxide electrolytes.

#### 4. Conclusions

In summary, we have predicted the atomic scale structure and electronic structure of misfit dislocations and oxygen vacancy defects in CeO<sub>2</sub>/MgO heterostructures. Thermodynamic stability of the CeO<sub>2</sub>/MgO interface offers fundamental interpretation of the mixed epitaxial relationship observed in experiments. Existence of different misfit dislocation structure along CeO<sub>2</sub>[110] and CeO<sub>2</sub>[100] shed light on the fundamental aspects of disparate bonding across the CeO<sub>2</sub>/MgO interface. Misfit dislocations at CeO<sub>2</sub>/MgO interface are more conducive for oxygen defect formation as compared to bulk and surfaces of ceria. Vacancy formation energies at Gddoped CeO<sub>2</sub>/MgO interface are exothermic in chemically frustrated regions across the interface due to unfavorable electrostatic interactions, whereas endothermic formation energies are uncovered in areas of favorable electrostatic interactions, which is likely to impact ionic transport across the interface. Oxygen vacancy is thermodynamically more favorable to occur at the interface layer of CeO<sub>2</sub> as compared to that of MgO. The electronic structure of oxygen vacancy in undoped CeO<sub>2</sub>/MgO interface reveal metal-induced gap states, whereas these gap

states disappear in Gd-doped CeO<sub>2</sub>/MgO owing to charge compensation via trivalent dopants. Strong interfacial chemical bonding is observed due to overlap of orbital signatures from various elements in the valence band. Interface electronic charge transfer mechanism from MgO to CeO<sub>2</sub> is witnessed for both defect-free and defective interfaces, wherein misfit dislocations play a fundamental role in interface stability and charge transfer. We have highlighted the significance of comprehending the atomic scale structure and electronic structure of misfit dislocations, which offer potential avenues to tune ionic transport in thin film oxide electrolytes.

## **Conflicts of interest**

There are no conflicts to declare.

**Supporting Information:** Interface layer atomic arrangement for relaxed geometries of vacancy configurations in CeO<sub>2</sub>/MgO heterostructure and density of states plots for three vacancy configurations.

## **Acknowledgments**

This work is supported by the National Science Foundation (NSF) CAREER Award grant number 2042311 in the Division of Materials Research. This work used Extreme Science and Engineering Discovery Environment (XSEDE), which is supported by NSF grant number ACI-1548562. We acknowledge partial computing resources from Research Computing at Rochester Institute of Technology.

#### References

<sup>&</sup>lt;sup>1</sup> Zubko, P.; Gariglio, S.; Gabay, M.; Ghosez, P.; Triscone, J. M. Interface Physics in Complex Oxide Heterostructures, *Annu. Rev. Cond. Matt. Phys.*, **2011**, *2*, 141.

<sup>&</sup>lt;sup>2</sup> Sulpizio, J. A.; Ilani, S.; Irvin, P.; Levy, J. Nanoscale Phenomena in Oxide Heterostructures, *Annu. Rev. Mater. Res.*, **2014**, *44*, 117.

<sup>&</sup>lt;sup>3</sup> Pryds, N.; Esposito, V. When two become one: An insight into 2D conductive oxide interfaces, *J. Electroceram.*, **2017**, *38*, 1.

<sup>&</sup>lt;sup>4</sup> Yu, P.; Chu, Y. H.; Ramesh, R. Oxide interfaces: pathways to novel phenomena, *Mater. Today*, **2012**, *15*, 320.

<sup>&</sup>lt;sup>5</sup> Huang, Z.; Ariando; Wang, X. R.; Rusydi, A.; Chen, J.; Yang, H.; Venkatesan, T. Interface Engineering and Emergent Phenomena in Oxide Heterostructures, *Adv. Mater.*, **2018**, *30*, 1802439.

<sup>&</sup>lt;sup>6</sup> Fabbri, E.; Pergolesi, D.; Traversa, E. Ionic conductivity in oxide heterostructures: the role of interfaces, *Sci. Tech. Adv. Mater.*, **2010**, *11*, 054503.

<sup>&</sup>lt;sup>7</sup> Garcia-Barriocanal, J.; Rivera-Calzada, A.; Varela, M.; Sefrioui, Z.; Iborra, E.; Leon, C.; Pennycook, S.J.; Santamaria, J. Colossal Ionic Conductivity at Interfaces of Epitaxial ZrO<sub>2</sub>:Y<sub>2</sub>O<sub>3</sub>/SrTiO<sub>3</sub> Heterostructures, *Science*, **2008**, *321*, 676.

<sup>&</sup>lt;sup>8</sup> Sillassen, M.; Eklund, P.; Pryds, N.; Johnson, E.; Helmersson, U.; Bøttiger, J. Low-temperature Superionic Conductivity in Strained Yttria-stabilized Zirconia, *Adv. Func. Mater.*, **2010**, *20*, 2071.

<sup>&</sup>lt;sup>9</sup> Zhang, F.; Cao, H.; Yue, D.; Zhang, J.; Qu, M. Enhanced Anode Performances of Polyaniline-TiO<sub>2</sub>-reduced Graphene Oxide Nanocomposites for Lithium Ion Batteries, *Inorgan. Chem.*, **2012**, *51*, 9544.

Jeen, H.; Choi, W. S.; Biegalski, M. D.; Folkman, C. M.; Tung, I. C.; Fong, D. D.; Freeland, J. W.; Shin, D.; Ohta, H.; Chisholm, M. F.; Lee, H. N. Reversible Redox Reactions in an Epitaxially Stabilized SrCoO<sub>x</sub> Oxygen Sponge, *Nat. Mater.*, 2013, *12*, 1057.

<sup>&</sup>lt;sup>11</sup> Assmann, E.; Blaha, P.; Laskowski, R.; Held, K.; Okamoto, S.; Sangiovanni, G. Oxide Heterostructures for Efficient Solar Cells, *Phys. Rev. Lett.*, **2013**, *110*, 078701.

<sup>&</sup>lt;sup>12</sup> Salluzzo, M.; Gariglio, S.; Stornaiuolo, D.; Sessi, V.; Rusponi, S.; Piamonteze, C.; De Luca, G. M.; Minola, M.; Marre, D.; Gadaleta, A. *et al.* Origin of Interface Magnetism in BiMnO<sub>3</sub>/SrTiO<sub>3</sub> and LaAlO<sub>3</sub>/SrTiO<sub>3</sub> Heterostructures, *Phys. Rev. Lett.*, **2013**, *111*, 087204.

<sup>13</sup> Hwang, H. Y.; Iwasa, Y.; Kawasaki, M.; Keimer, B.; Nagaosa, N.; Tokura, Y. Emergent Phenomena at Oxide Interfaces, *Nat. Mater.*, **2012**, *11*, 103.

- <sup>14</sup> Pennycook, S.; Zhou, H.; Chisholm, M.; Borisevich, A.; Varela, M.; Gazquez, J.; Pennycook, T.; Narayan, J. Misfit Accommodation in Oxide Thin Film Heterostructures, *Acta Mater.*, **2013**, *61*, 2725.
- <sup>15</sup> Schichtel, N.; Korte, C.; Hesse, D.; Janek, J. Elastic Strain at Interfaces and its Influence on Ionic Conductivity in Nanoscaled Solid Electrolyte Thin Films Theoretical Considerations and Experimental Studies, *Phys. Chem. Chem. Phys.*, **2009**, *11*, 3043.
- <sup>16</sup> Peters, A.; Korte, C.; Hesse, D.; Zakharov, N.; Janek, J. Ionic Conductivity and Activation Energy for Oxygen Ion Transport in Superlattices—The Multilayer System CSZ (ZrO<sub>2</sub>+CaO)/Al<sub>2</sub>O<sub>3</sub>, *Solid State Ion.*, **2007**, *178*, 67.
- <sup>17</sup> Sadykov, V.; Usoltsev, V.; Yeremeev, N.; Mezentseva, N.; Pelipenko, V.; Krieger, T.; Belyaev, V.; Sadovskaya, E.; Muzykantov, V.; Fedorova, Y. *et al.* Functional Nanoceramics for Intermediate Temperature Solid Oxide Fuel cells and Oxygen Separation Membranes, *J. Euro. Ceram. Soc.*, **2013**, *33*, 2241.
- <sup>18</sup> Lee, S.; Zhang, W.; Khatkhatay, F.; Wang, H.; Jia, Q.; MacManus-Driscoll, J. L. Ionic Conductivity Increased by Two Orders of Magnitude in Micrometer-Thick Vertical Yttria-Stabilized ZrO<sub>2</sub> Nanocomposite Films, *Nano Lett.*, **2015**, *15*, 7362.
- <sup>19</sup> Kosacki, I.; Rouleau, C. M.; Becher, P. F.; Bentley, J.; Lowndes, D. H. Nanoscale Effects on the Ionic Conductivity in Highly Textured YSZ Thin Films, *Solid State Ion.*, **2005**, *176*, 1319.
- <sup>20</sup> Pergolesi, D.; Fronzi, M.; Fabbri, E.; Tebano, A.; Traversa, E. Growth mechanisms of ceriaand zirconia-based epitaxial thin films and hetero-structures grown by pulsed laser deposition, *Mater. Renew. Sust. Energy*, **2012**, *2*, 6.
- <sup>21</sup> Saito, Y.; Cheng, J.; Crabb, K.; Huang, H.; Pornprasertsuk, R.; Su, P. C.; Prinz, F. Ion Conductivity Enhancement Effect by Introduction of Dislocations in Yttria-stabilized Zirconia, *ECS Trans.*, **2008**, *11*, 3.
- <sup>22</sup> Guo, X. *Science*, Comment on Colossal Ionic Conductivity at Interfaces of Epitaxial ZrO<sub>2</sub>:Y<sub>2</sub>O<sub>3</sub>/SrTiO<sub>3</sub> Heterostructures, **2009**, *324*, 465.
- <sup>23</sup> Harrington, G. F.; Cavallaro, A.; McComb, D. W.; Skinner, S. J.; Kilner, J. A. The Effects of Lattice Strain, Dislocations, and Microstructure on the Transport Properties of YSZ Films, *Phys. Chem. Chem. Phys.*, **2017**, *19*, 14319.
- <sup>24</sup> Dholabhai, P. P.; Martinez, E.; Brown, N. T.; Uberuaga, B. P. On the Mobility of Carriers at Semi-coherent Oxide Heterointerfaces, *Phys. Chem. Chem. Phys.*, **2017**, *19*, 23122.

<sup>25</sup> Dholabhai, P. P.; Pilania, G.; Aguiar, J. A.; Misra, A.; Uberuaga, B. P. Termination Chemistry-driven Dislocation Structure at SrTiO<sub>3</sub>/MgO Heterointerfaces, *Nat. Commun.*, **2014**, *5*, 5043.

- <sup>26</sup> Dholabhai, P. P.; Aguiar, J. A.; Misra, A.; Uberuaga, B. P. Defect Interactions with Stepped CeO<sub>2</sub>/SrTiO<sub>3</sub> Interfaces: Implications for Radiation Damage Evolution and Fast Ion Conduction, *J. Chem. Phys.*, **2014**, *140*, 194701.
- <sup>27</sup> Aguiar, J. A.; Dholabhai, P. P.; Bi, Z.; Jia, Q.; Fu, E.; Wang, Y.; Aoki, T.; Zhu, J.; Misra, A.; Uberuaga, B. P. Linking Interfacial Step Structure and Chemistry with Locally Enhanced Radiation-Induced Amorphization at Oxide Heterointerfaces, *Adv. Mater. Inter.* **2014**, *1*, 1300142.
- <sup>28</sup> Nagarajan, V.; Jia, C. L.; Kohlstedt, H.; Waser, R.; Misirlioglu, I. B.; Alpay, S. P.; Ramesh, R. Misfit dislocations in nanoscale ferroelectric heterostructures, *Appl. Phys. Lett.*, **2005**, *86*, 192910.
- <sup>29</sup> Xu, Y. B.; Tang, Y. L.; Zhu, Y. L.; Liu, Y.; Li, S.; Zhang, S. R.; Ma, X. L. Misfit Strain Relaxation of Ferroelectric PbTiO3/LaAlO3 (111) Thin Film System, *Sci. Rep.*, **2016**, *6*, 35172.
- <sup>30</sup> Lee, W. J.; Kim, H. J.; Kang, J.; Jang, D. H.; Kim, T. H.; Lee, J. H.; Kim, K. H. Transparent Perovskite Barium Stannate with High Electron Mobility and Thermal Stability, *Annu. Rev. Mater. Res.*, **2017**, *47*, 391.
- <sup>31</sup> Bagués, N.; Santiso, J.; Esser, B. D.; Williams, R. E. A.; McComb, D. W.; Konstantinovic, Z.; Balcells, L.; Sandiumenge, F. The misfit dislocation core phase in complex oxide heteroepitaxy, *Adv. Func. Mater.*, **2018**, *28*, 1704437.
- <sup>32</sup> Yildiz, B. Stretching the Energy Landscape of Oxides Effects on Electrocatalysis and Diffusion, *MRS Bulletin*, **2014**, *39*, 147.
- <sup>33</sup> Sandiumenge, F. Strain Landscapes and Self-organization of Free Surfaces in Complex Oxide Epitaxy, *J. Mater. Res.*, **2017**, *32*, 3958.
- <sup>34</sup> Jaiswal, A.; Pesaran, A.; Omar, S.; Wachsman, E. D. Ceria/Bismuth Oxide Bilayer Electrolyte Based Low-Temperature SOFCs with Stable Electrochemical Performance, *ECS Transac.*, **2017**, 78, 361.
- <sup>35</sup> Wachsman, E. D.; Lee, K. T. Lowering the Temperature of Solid Oxide Fuel Cells, *Science*, **2011**, *334*, 935.
- <sup>36</sup> Kilner, J. A.; Burriel, M. Materials for Intermediate-Temperature Solid-Oxide Fuel Cells, *Annu. Rev. Mater. Res.* **2014**, *44*, 11.1–11.29.

<sup>37</sup> Brett, D. J. L.; Atkinson, A.; Brandon, N. P.; Skinner, S. J. Intermediate temperature solid oxide fuel cells, *Chem. Soc. Rev.*, **2008**, *37*, 1568.

- <sup>38</sup> Li, B.; Zhang, J.; Kaspar, T.; Shutthanandan, V.; Ewing. R. C.; Lian, J. Multilayered YSZ/GZO films with greatly enhanced ionic conduction for low temperature solid oxidefuel cells, *Phys. Chem. Chem. Phys.*, **2013**, *15*, 1296.
- <sup>39</sup> Guo, X.; Vasco, E.; Mi, S.; Szot, K.; Wachsman, E.; Waser, R. Ionic Conduction in Zirconia Films of Nanometer Thickness, *Acta Mater.*, **2005**, *53*, 5161.
- <sup>40</sup> Sun, L.; Marrocchelli, D.; Yildiz, B. Edge Dislocation Slows Down Oxide Ion Diffusion in Doped CeO<sub>2</sub> by Segregation of Charged Defects, *Nat. Commun.*, **2015**, *6*, 6294.
- <sup>41</sup> Metlenko, V.; Ramadan, A. H. H.; Gunkel, F.; Du, H.; Schraknepper, H.; Hoffmann-Eifert, S.; Dittmann, R.; Waser, R.; De Souza, R. A. Do Dislocations Act as Atomic Autobahns for Oxygen in the Perovskite Oxide SrTiO<sub>3</sub>, *Nanoscale*, **2014**, *6*, 12864.
- <sup>42</sup> Andersson, D. A.; Simak, S. I.; Skorodumova, N. V.; Abrikosov, I. A.; Johansson, B. Optimization of Ionic Conductivity in Doped Ceria, *Proc. Nat. Acad. Sci.*, **2006**, *103*, 3518.
- <sup>43</sup> Dholabhai, P. P.; Adams, J. B.; Crozier, P.; Sharma, R. Oxygen Vacancy Migration in Ceria and Pr-doped Ceria: A DFT+*U* Study, *J. Chem. Phys.*, **2010**, *132*, 094104.
- <sup>44</sup> Dholabhai, P. P.; Adams, J. B.; Crozier, P.; Sharma, R. A Density Functional Study of Defect Migration in Gadolinium Doped Ceria, *Phys. Chem. Chem. Phys.*, **2010**, *12*, 7904.
- <sup>45</sup> Tuller, H. L.; Nowick, A. S. Doped Ceria as a Solid Oxide Electrolyte, *J. Electrochem. Soc.*, **1975**, *122*, 255.
- <sup>46</sup> Steele, B. C. H. Appraisal of Ce<sub>1-y</sub>Gd<sub>y</sub>O<sub>2-y/2</sub> electrolytes for IT-SOFC operation at 500°C, *Solid State Ion.*, **2000**, *129*, 95.
- <sup>47</sup> Tuller, H. L. Ionic Conduction in Nanocrystalline Materials, *Solid State Ion.*, **2000**, *131*, 143.
- <sup>48</sup> Mogensen, M.; Sammes, N. M.; Tompsett, G. A. Physical, Chemical and Electrochemical Properties of Pure and Doped Ceria, *Solid State Ion.*, **2000**, *129*, 63.
- <sup>49</sup> Omar, S.; Wachsman, E. D.; Nino, J. C. Higher Ionic Conductive Ceria Based Electrolytes for SOFCs, *Appl. Phys. Lett.*, **2007**, *91*, 1444106.
- <sup>50</sup> Steele, B. C. H.; Heinzel, A. Materials for Fuel-cell Technologies, *Nature*, **2001**, *414*, 345.
- <sup>51</sup> Dholabhai, P. P.; Anwar, S.; Adams, J. B.; Crozier, P.; Sharma, R. Kinetic Lattice Monte Carlo Model for Oxygen Vacancy Diffusion in Praseodymium Doped Ceria: Applications to Materials Design, *J. Solid State Chem.*, **2011**, *184*, 811.

<sup>52</sup> Nakayama, N.; Martin, M. First-principles Study on Defect Chemistry and Migration of Oxide Ions in Ceria Doped with Rare-earth Cations, *Phys. Chem. Chem. Phys.*, **2009**, *11*, 3241.

- <sup>53</sup> Grieshammer, S.; Grope, B. O. H.; Koettgen, J.; Martin, M. A combined DFT + U and Monte Carlo study on rare earth doped ceria, *Phys. Chem. Chem. Phys.*, **2014**, *16*, 9974.
- <sup>54</sup> Grieshammer, S.; Nakayama, N.; Martin, M. Association of defects in doped non-stoichiometric ceria from first principles, *Phys. Chem. Chem. Phys.*, **2016**, *18*, 3804.
- <sup>55</sup> Grieshammer, S.; Martin, M. Influence of defect interactions on the free energy of reduction in pure and doped ceria, *J. Mater. Chem. A*, **2017**, *5*, 9241.
- <sup>56</sup> Koettgen, J.; Schmidt, P. C.; Bucko, T.; Martin, M. Ab initio calculation of the migration free energy of oxygen diffusion in pure and samarium-doped ceria, *Phys. Rev. B*, **2018**, *97*, 024305.
- <sup>57</sup> Koettgen, J.; Grieshammer, S.; Hein, P.; Grope, B. O. H.; Nakayama, N.; Martin, M. Understanding the ionic conductivity maximum in doped ceria: trapping and blocking, *Phys. Chem. Chem. Phys.*, **2018**, *20*, 14291.
- <sup>58</sup> Koettgen, J.; Martin, M. Coordination Numbers in Sm-Doped Ceria Using X-ray Absorption Spectroscopy, *J. Phys. Chem. C*, **2019**, *123*, 6333.
- <sup>59</sup> Dholabhai, P. P.; Anwar, S.; Adams, J. B.; Crozier, P.; Sharma, R. Predicting the Optimal Dopant Concentration in Gadolinium Doped Ceria: A Kinetic Lattice Monte Carlo Approach, *Modelling Simul. Mater. Sci. Eng.* **2012**, *20*, 015004.
- <sup>60</sup> Dholabhai, P. P.; Adams, J. B. A Blend of First-principles and Kinetic Lattice Monte Carlo Computation to Optimize Samarium-doped Ceria, *J. Mater. Sci.* **2012**, *47*, 7530.
- <sup>61</sup> Hirai, K.; Aso, R.; Ozaki, Y.; Kan, D.; Haruta, M.; Ichikawa, N.; Kurata, H.; Shimakawa, Y. Melting of Oxygen Vacancy Order at Oxide–Heterostructure Interface, *ACS Appl. Mater. Inter.*, **2017**, *9*, 30143.
- <sup>62</sup> Dholabhai, P. P.; Martinez, E.; Uberuaga, B. P. Influence of Chemistry and Misfit Dislocation Structure on Dopant Segregation at Complex Oxide Heterointerfaces, *Adv. Theory Simul.*, **2019**, *2*, 1800095.
- <sup>63</sup> Cheah, W. L.; Finnis, M. W. Structure of multilayer ZrO<sub>2</sub>/SrTiO<sub>3</sub>, *J. Mater. Sci.*, **2012**, *47*, 1631.
- <sup>64</sup> Abutaha, A. I.; Sarath Kumar, S. R.; Mehdizadeh Dehkordi, A.; Tritt, T. M.; Alshareef, H. N. Doping site dependent thermoelectric properties of epitaxial strontium titanate thin films, *J. Mater. Chem. C*, **2014**, *2*, 9712.
- <sup>65</sup> Aparicio-Angles, X.; de Leeuw, N. H. Modeling of complex interfaces: Gadolinium-doped ceria in contact with yttria-stabilized zirconia, *J. Am. Ceram. Soc.*, **2017**, *100*, 3329.

- <sup>66</sup> Veal, B. W.; Kim, S. K.; Zapol, P.; Iddir, H.; Baldo, P. M.; Eastman, J. A. Interfacial control of oxygen vacancy doping and electrical conduction in thin film oxide heterostructures, *Nature Comm.*, **2016**, *7*, 11892.
- <sup>67</sup> Herranz, G.; Basletic, M.; Bibes, M.; Carretero, C.; Tafra, E.; Jacquet, E.; Bouzehouane, K.; Deranlot, C.; Hamzic, A.; Broto, J.-M.; Barthelemy, A.; Fert, A. High Mobility in LaAlO<sub>3</sub>/SrTiO<sub>3</sub> Heterostructures: Origin, Dimensionality, and Perspectives, *Phys. Rev. Lett.*, **2007**, *98*, 216803.
- <sup>68</sup> Zhang, Y. Y.; Mishra, R.; Pennycook, T. J.; Borisevich, A. Y.; Pennycook, S. J.; Pantelides, S. T. Oxygen Disorder, a Way to Accommodate Large Epitaxial Strains in Oxides, *Adv. Mater. Inter.*, **2015**, *2*, 1500344.
- <sup>69</sup> Li, Z.-P.; Mori, T.; Ye, F.; Ou, D.; Zou, J.; Drennan, J. Ordered structures of defect clusters in gadolinium-doped ceria, *J. Chem. Phys.* **2011**, *134*, 224708.
- <sup>70</sup> Chen, L.; Chen, C. L.; Chen, X.; Donner, W.; Liu, S. W.; Lin, Y.; Huang, D. X.; Jacobson, A. J. Electrical properties of a highly oriented, textured thin film of the ionic conductor  $Gd:CeO2-\delta$   $Gd:CeO2-\delta$  on (001) MgO, *Appl. Phys. Lett.*, **2003**, *83*, 4737.
- <sup>71</sup> Copetti, C. A.; Schubert, J.; Klushin, A. M.; Bauer, S.; Zander, W.; Buchal, Ch.; Seo, J. W.; Sanchez, F.; Bauer, M. Graphoepitaxy of CeO<sub>2</sub> on MgO and its Application to the Fabrication of 45° Grain Boundary Josephson Junctions of YBa<sub>2</sub>Cu<sub>3</sub>O<sub>7-x</sub>, *J. Appl. Phys.*, **1995**, *78*, 5058.
- <sup>72</sup> Fluri, A.; Pergolesi, D.; Roddatis, V.; Wokaun, A.; Lippert, T. In Situ Stress Observation in Oxide Films and how Tensile Stress Influences Oxygen Ion Conduction, *Nat. Comm.*, **2016**, 7, 10692.
- <sup>73</sup> Zhao, P.; Huang, Z.; Mao, Y.; Wang,Y.; Takashi, G. Preparation of (100)-oriented CeO2 film on (100) MgO single crystal substrate by laser chemical vapor deposition using solid precursor, *Ceram. Inter.*, **2014**, *40*, 15919.
- <sup>74</sup> Sanna, S.; Esposito, V.; Andreasen, J. W.; Hjelm, J.; Zhang, W.; Kasama, T.; Simonsen, S. B.; Christensen, M.; Linderoth, S.; Pryds, N. Enhancement of the chemical stability in confined δ-Bi2O3, *Nat. Mater.*, **2015**, *14*, 500.
- <sup>75</sup> Perez Casero, R.; Gomez San Roman, R.; Perriere, J.; Laurent, A.; Seiler, W.; Gergaud, P.; Keller, D. Epitaxial growth of CeO2 on MgO by pulsed laser deposition, *Appl. Surf. Sci.*, **1997**, *109*/110, 341.
- <sup>76</sup> Dholabhai, P. P.; Uberuaga, B. P. Beyond Coherent Oxide Heterostructures: Atomic-scale Structure of Misfit Dislocations, *Adv. Theory Simul.*, **2019**, *2* (9), 1900078.

<sup>77</sup> Cheng, C.; Kunc, K.; Kresse, G.; Hafner, J. SrTiO<sub>3</sub>/MgO(001) and MgO/SrTiO<sub>3</sub>(001) Systems: Energetics and Stresses, *Phys. Rev. B*, **2002**, *66*, 085419.

- <sup>78</sup> Casek, P.; Bouette-Russo, S.; Finocchi, F.; Noguera, C.; SrTiO<sub>3</sub>(001) Thin Films on MgO(001): A Theoretical Study, *Phys. Rev. B*, **2004**, *69*, 085411.
- <sup>79</sup> Pennycook, T. J.; Beck, M. J.; Varga, K.; Varela, M.; Pennycook, S. J.; Pantelides, S. T. Origin of Colossal Ionic Conductivity in Oxide Multilayers: Interface Induced Sublattice Disorder, *Phys. Rev. Lett.*, **2010**, *104*, 115901.
- <sup>80</sup> Dholabhai, P. P. Atomic-scale Structure of Misfit Dislocations in CeO<sub>2</sub>/MgO Heterostructure and Thermodynamic Stability of Dopant-defect Complexes at the Heterointerface, *Phys. Chem. Chem. Phys.*, **2019**, *21*, 20878.
- 81 Hohenberg, P.; Kohn, W. Inhomogeneous Electron Gas, Phys. Rev., 1964, 136, B864.
- <sup>82</sup> Kohn, W.; Sham, L. J. Self-Consistent Equations Including Exchange and Correlation Effects, *Phys. Rev.* **1965**, *140*, A1133.
- <sup>83</sup> Perdew, J. P.; Burke, K.; Ernzerhof, M. Generalized Gradient Approximation Made Simple, *Phys. Rev. Lett.*, **1996**, *77*, 3865.
- <sup>84</sup> Bhöchl, P. E. Projector augmented-wave method, *Phys. Rev. B*, **1994**, *50*, 17953.
- <sup>85</sup> Kresse, G.; Hafner, J. Ab Initio Molecular Dynamics for Liquid Metals, *Phys. Rev. B*, **1993**, 47, 558.
- <sup>86</sup> Kresse, G.; Furthmuller, J. Efficient Iterative Schemes for Ab Initio Total-energy Calculations Using a Plane-wave Basis Set, *Phys. Rev. B*, **1996**, *54*, 11169.
- <sup>87</sup> Dudarev, S. L.; Botton, G. A.; Savrasov, S. Y.; Humphreys, C. J.; Sutton, A. P. Electronenergy-loss Spectra and the Structural Stability of Nickel Oxide: An LSDA+*U* Study, *Phys. Rev. B* **1998**, *57*, 1505–1509.
- <sup>88</sup> Monkhorst, H. J.; Pack, J. D. Special points for Brillouin-zone integrations, *Phys. Rev. B*, **1976**, *13*, 5188.
- <sup>89</sup> Towns, J.; Cockerill, T.; Dahan, M.; Foster, I.; Gaither, K.; Grimshaw, A.; Hazlewood, V.; Lathrop, S.; Lifka, D.; Peterson, G. D. *et al.* "XSEDE: Accelerating Scientific Discovery", Computing in Science & Engineering, vol.16, no. 5, pp. 62-74, Sept.-Oct. 2014, doi:10.1109/MCSE.2014.80
- <sup>90</sup> Berland, K.; Cooper, V. R.; Lee, K.; Schröder, E.; Thonhauser, T.; Hyldgaard, P.; Lundqvist, B. I. *Rep. Prog. Phys.*, **2015**, *78*, 066501.
- <sup>91</sup> Choudhury, S.; Morgan, D.; Uberuaga, B. P. Massive Interfacial Reconstruction at Misfit Dislocations in Metal/Oxide Interfaces, *Sci. Rep.* **2014**, *4*, 6533.

- <sup>92</sup> Shutthanandan, V.; Choudhury, S.; Manandhar, S.; Kaspar, T. C.; Wang, C.; Devaraj, A.; Wirth, B. D.; Thevuthasan, S.; Hoagland, R. G.; Dholabhai, P. P. *et al.* Radiation Tolerant Interfaces: Influence of Local Stoichiometry at the Misfit Dislocation on Radiation Damage Resistance of Metal/Oxide Interfaces, *Adv. Mater. Inter.*, **2017**, *4*, 1700037.
- <sup>93</sup> Rébola, A.; Fong, D. D.; Eastman, J. A.; Öğüt, S.; Zapol, P. First-principles Study of Compensation Mechanisms in Negatively Charged LaGaO<sub>3</sub>/MgAl<sub>2</sub>O<sub>4</sub> Interfaces, *Phys. Rev. B*, **2013**, *87*, 245117.
- <sup>94</sup> Shannon, R. D. Revised effective ionic radii and systematic studies of interatomic distances in halides and chalcogenides, *Acta Crystallogr.*, *Sect. A: Cryst. Phys.*, *Diffr.*, *Theor. Gen. Crystallogr.*, **1976**, *32*, 751.
- <sup>95</sup> Nolan, M.; Fearon, J. E.; Watson, G. W. Oxygen vacancy formation and migration in ceria, *Solid State. Ion.*, **2006**, *177*, 3069.
- <sup>96</sup> Yang, Z.; Ma, D. W.; Yu, X. H.; Hermansson, K. The main factors influencing the O vacancy formation on the Ir doped ceria surface: A DFT+U study, *Eur. Phys. J. B*, **2010**, *77*, 373.
- <sup>97</sup> Yang, Z.; Luo, G.; Lu, Z.; Hermansson, K. Oxygen vacancy formation energy in Pd-doped ceria: DFT+U study, *J. Chem. Phys.*, **2007**, *127*, 074704.
- <sup>98</sup> Yang, Z.; Woo, T. K.; Hermansson, K. Effects of Zr doping on stoichiometric and reduced ceria: A first-principles study, *J. Chem. Phys.*, **2006**, *124*, 224704.
- <sup>99</sup> Ganduglia-Pirovano, M. V.; Da Silva, J. L. F.; Sauer, J. Density-Functional Calculations of the Structure of Near-Surface Oxygen Vacancies and Electron Localization on CeO2(111), *Phys. Rev. Lett.*, **200**9, *102*, 026101
- <sup>100</sup> Nolan, M. Enhanced oxygen vacancy formation in ceria (111) and (110) surfaces doped with divalent cations, *J. Mater. Chem.*, **2011**, *21*, 9160.
- <sup>101</sup> Nolan, M.; Parker, S. C.; Watson, G. W.; The electronic structure of oxygen vacancy defects at the low index surfaces of ceria, *Surf. Sci.*, **2005**, *595*, 223.
- <sup>102</sup> Nolan, M. Charge Compensation and Ce3+ Formation in Trivalent Doping of the CeO2(110) Surface: The Key Role of Dopant Ionic Radius, *J. Phys. Chem. C*, **2011**, *115*, 6671.
- <sup>103</sup> Paier, J.; Penschke, C.; Sauer, J. Oxygen Defects and Surface Chemistry of Ceria: Quantum Chemical Studies Compared to Experiment, *Chem. Rev.*, **2013**, *113*, 3949.
- <sup>104</sup> Navrotsky, A.; Simoncic, P.; Yokokawa, H.; Chen, W.; Lee, T. Calorimetric measurements of energetics of defect interactions in fluorite oxides, *Faraday Discuss.*, **2007**, *134*, 171.

<sup>105</sup> Aparicio-Angles, X.; Roldan, A.; de Leeuw, N. H. Gadolinium-Vacancy Clusters in the (111) Surface of Gadolinium-Doped Ceria: A Density Functional Theory Study, *Chem. Mater.*, **2015**, *27*, 7910.

<sup>106</sup> Bader, R. F. W., "A quantum theory of molecular structure and its applications", *Chem. Rev.* **1991**, *91*, 36.

<sup>107</sup> Henkelman, G.; Arnaldsson, A.; Jonsson, H. A fast and robust algorithm for Bader decomposition of charge density. *Comput. Mater. Sci.* **2006**, *36*, 354.